Multi-wavelength analysis of the luminous GRB 210619B observed with *Fermi* and ASIM: a transition between thermal to non-thermal outflow?

M. D. Caballero-García[1]⋆, Rahul Gupta[2,3]†, S. B. Pandey[2], S. R. Oates[4], M. Marisaldi[5,6], Y.-D. Hu[1],
A. J. Castro-Tirado[1,7], R. Sánchez-Ramírez[1], P. H. Connell[8], F. Christiansen[9], A. Kumar Ror[2],
A. Aryan[2,3], J.-M. Bai[10], M. A. Castro-Tirado[1,7], Y.-F. Fan[10], E. Fernández-García[1], A. Kumar[2,11],
A. Lindanger[5], A. Mezentsev[5], J. Navarro-González[8], T. Neubert[9], N. Østgaard[5], I. Pérez-García[1],
V. Reglero[8], D. Sarria[5], T. R. Sun[1], D.-R. Xiong[10], J. Yang[12], Y.-H. Yang[12], and B.-B. Zhang[12,13]

[1] *Instituto de Astrofísica de Andalucía (IAA-CSIC), Glorieta de la Astronomía s/n, E-18008, Granada*
[2] *Aryabhatta Research Institute of Observational Sciences (ARIES), Manora Peak, Nainital-263002, India*
[3] *Department of Physics, Deen Dayal Upadhyaya Gorakhpur University, Gorakhpur-273009, India*
[4] *School of Physics and Astronomy & Institute for Gravitational Wave Astronomy, University of Birmingham, B15 2TT, UK*
[5] *Birkeland Centre for Space Science, Department of Physics and Technology, University of Bergen, Norway*
[6] *National Institute for Astrophysics, Osservatorio di Astrofisica e Scienza dello Spazio, Bologna, Italy*
[7] *Unidad Asociada al CSIC, Departamento de Ingeniería de Sistemas y Automática, Escuela de Ingenierías, Universidad de Málaga, Málaga, Spain*
[8] *Image Processing Laboratory, University of Valencia, Paterna, Valencia, Spain*
[9] *National Space Institute, Technical University of Denmark, Kgs. Lyngby, Denmark*
[10] *Yunnan Observatories, Chinese Academy of Sciences, Kunming, 650216, China*
[11] *School of Studies in Physics and Astrophysics, Pandit Ravishankar Shukla University, Raipur, Chattisgarh-492010, India*
[12] *School of Astronomy and Space Science, Nanjing University, Nanjing 210093, China*
[13] *Key Laboratory of Modern Astronomy and Astrophysics (Nanjing University), Ministry of Education, Nanjing 210093, China*

ABSTRACT

We report on detailed **multi-wavelength** observations and analysis of the very bright and long GRB 210619B, detected by the Atmosphere-Space Interactions Monitor (ASIM) installed on the International Space Station (*ISS*) and the Gamma-ray Burst Monitor (GBM) on-board the *Fermi* mission. Our main goal is to understand the radiation mechanisms and jet composition of GRB 210619B. With a measured redshift of $z = 1.937$, we find that GRB 210619B falls within the 10 most luminous bursts observed by *Fermi* so far. The energy-resolved prompt emission light curve of GRB 210619B exhibits an extremely bright hard emission pulse followed by softer/longer emission pulses. The low-energy photon indices ($\alpha_{\rm pt}$) values obtained using the time-resolved spectral analysis of the burst reveal a transition between the thermal (during harder pulse) to non-thermal (during softer pulse) outflow. We examine the correlation between spectral parameters and find that both peak energy and $\alpha_{\rm pt}$ exhibit the flux tracking pattern. The late time broadband photometric dataset can be explained within the framework of the external forward shock model with $\nu_m < \nu_c < \nu_x$ (where ν_m, ν_c, and ν_x are the synchrotron peak, cooling-break, and X-ray frequencies, respectively) spectral regime supporting a rarely observed hard electron energy index ($p < 2$). We find moderate values of host extinction of E(B-V) = 0.14 ± 0.01 mag for the Small Magellanic Cloud (SMC) extinction law. In addition, we also report late-time optical observations with the 10.4 m GTC placing deep upper limits for the host galaxy (z=1.937), favouring a faint, dwarf host for the burst.

Key words: gamma-ray burst: general, gamma-ray burst: individual: GRB 210619B, methods: data analysis

1 INTRODUCTION

Gamma-ray bursts (GRBs) are the brightest and most explosive electromagnetic transients in the Universe. GRBs originate at cosmological distances with energy releases of $10^{51} – 10^{53}$ erg s^{-1} and are not well-understood in terms of physical models more than five decades after their serendipitous discovery (Klebesadel et al. 1973; Kumar &

Zhang 2015). The multi-wavelength emission (from very high energy through to the radio) that follows the gamma-ray emission (the "afterglow") partly satisfies the predictions of the "standard" relativistic fireball model (Meszaros & Rees 1993).

The progenitors that produce the long-duration (> 2 s) GRBs are considered to be the collapse of massive stars (Woosley 1993; Hjorth et al. 2003; Campana et al. 2006). They are believed to be powered by a central engine (stellar-mass black holes or millisecond magnetars; Petropoulou et al. 2020). Furthermore, optical/near-IR studies of GRB afterglows and their hosts have provided insight into key

⋆ E-mail: mcaballero@iaa.es
† E-mail: rahulbhu.c157@gmail.com

aspects related to their underlying physical mechanisms and possible progenitors.

GRB prompt emission is observed when the relativistic jets dissipate the energy and accelerate the particles either via internal shocks or magnetic reconnection (Pe'er 2015). These processes radiate and provide a non-thermal spectrum, probably synchrotron radiation (Burgess et al. 2020; Zhang 2020). However, synchrotron emission is not consistent with the observed spectra for a large number of GRBs (Pe'er 2015; Zhang 2014). The key feature of the prompt emission spectra of GRBs is the sub-MeV peak, which can be explained well using the empirical Band function (Band et al. 1993). In addition to non-thermal synchrotron emission (Band) originated at the optically thin region, a quasi-thermal blackbody component (produced by the photosphere) is also observed in some GRBs (Ryde 2005; Guiriec et al. 2011; Zhang 2014). According to the classical fireball model, initially, the jetted outflow is optically thick, and due to expansion, the flow becomes transparent at a certain point (also known as photospheric radius, r_{ph}), and thermal radiation emitted towards the observer, results as a subdominant/dominant part of the entire observed prompt gamma-ray spectra (Beloborodov & Mészáros 2017). Moreover, some spectra show a few additional features, such as a sub-GeV spectral cut-off (Vianello et al. 2018; Chand et al. 2020), a low energy break in the spectrum (Ravasio et al. 2019; Gupta et al. 2022), and multiple components (Tak et al. 2019). Thus, it is challenging to explain the radiation physics of GRBs using a single model (different spectral components are associated with different emissions originated at different regions).

Time-resolved spectral analysis is a unique method for understanding the temporal evolution of modelled spectral parameters and also providing insights into the origin of the prompt emission (Pe'er 2015). The prompt light curve of GRBs generally consists of multiple pulses produced by irregular central engine activity or multiple internal shocks, and the temporal evolution of spectral parameters (mainly peak energy, E_p) among the pulses. There are four possible patterns of E_p evolution reported in the literature: (i) 'soft-to-hard (STH)' pattern, where E_p becomes harder with time (Kargatis et al. 1994); (ii) 'hard-to-soft (HTS)' pattern, where E_p becomes softer with time (Norris et al. 1986); (iii) 'flux-tracking (FT)' pattern, where E_p becomes harder when the flux increases or vice versa (Ryde & Svensson 1999); (iv) random pattern, where E_p evolves randomly (Kargatis et al. 1994). The evolution pattern of E_p has been used to explain the observed spectral lag in the bursts light curves (Uhm et al. 2018). In addition to E_p evolution, the low energy power-law index (α_{pt}) also varies over time; however, it does not have any particular pattern (Crider et al. 1997). Recently, Yu et al. (2019) studied 37 single pulses of 38 GRBs observed by *Fermi* GBM till 2018 and found that most of the individual pulses ($\sim 60\%$) have a harder α_{pt} than the synchrotron line of death (α_{pt} = -2/3, i.e. LOD; Preece et al. 1998). More recently, Li et al. (2021) performed the time-resolved spectral analysis of multi-pulsed GRBs observed by *Fermi* GBM and found that the typical pattern of the pulses becomes softer with time, mostly with α_{pt} becoming smaller, suggesting a transition from the photosphere to synchrotron emission. For some bright bursts, some authors (Li et al. 2019; Gupta et al. 2021, 2022) examined the evolution pattern of spectral parameters and noticed that E_p and α_{pt} both show a flux tracking ("double-tracking") behavior.

In this paper, we studied in detail the prompt emission and afterglow through the analysis of one of the most luminous bursts (GRB 210619B). It was promptly detected by the Modular X- and Gamma-ray Sensor (Østgaard et al. 2019) on the Atmosphere-Space Interactions Monitor (*ASIM*; Neubert et al. 2019) installed on the International Space Station (*ISS*) and the Gamma-ray Burst Monitor

(GBM; Meegan et al. 2009) onboard the *Fermi* mission. The GBM discovered this bright and long GRB which was also observed by ASIM.

We also report our optical follow-up observations using many observatories, including the host galaxy search from the observations with the *Gran Telescopio de Canarias* (10.4 m) GTC (Canary Islands, Spain). This GRB detection by ASIM (plus *Swift*-BAT and *Fermi*-GBM) having peculiar properties along with the late-time optical follow-up observations using the 10.4 m GTC motivated us for a detailed analysis of this luminous GRB 210619B.

The paper is organized as follows. In § 2, we give the details of **high energy** observations, data analysis, **results, and discussion of the prompt emission of GRB 210619B**. In § 3, we give the details of **broadband** observations, data analysis, **results, and discussion of the afterglow of GRB 210619B**. Finally, a brief summary and conclusion is given in § 4. We used a standard cosmology model (H_0 = 70 km s^{-1} Mpc^{-1}, Ω_M = 0.27, and Ω_λ = 0.73) to calculate the restframe parameters.

2 HIGH ENERGY EMISSION OF GRB 210619B

2.1 Observations and data analysis

GRB 210619B was initially detected by the Gamma-Ray Burst Monitor (GBM) and the Burst Alert Telescope (BAT; Barthelmy et al. 2005), being on-board the *Fermi* and *Swift* satellites, respectively (Poolakkil et al. 2021; D'Avanzo et al. 2021a). This section presents the **prompt** observational **, and data analysis details** carried out by *Fermi*, ASIM-*ISS*, and *Swift* **missions**.

2.1.1 Fermi *GBM*

The *Fermi* GBM detected GRB 210619B (see the light curve in Figure 1) at 23:59:25.60 UT on 19 June 2021 (Poolakkil et al. 2021). We used the time-tagged events (TTE) mode *Fermi* GBM data[1] for the temporal and spectral analysis of GRB 210619B. The TTE mode observations have a good temporal and spectral resolution. For the GBM temporal and spectral analysis, we considered the three brightest sodium iodide (NaI) and one of the brightest bismuth germanate (BGO) detectors. We have used RMFIT version 4.3.2 software[2] to create the prompt emission light curve of GRB 210619B in different energy channels. The background-subtracted *Fermi* GBM light curve of GRB 210619B in different energy channels along with the hardness-ratio (HR) evolution is shown in Figure 1. The shaded region in Figure 1 shows the time-interval (T_0 to T_0 +67.38 s) for the time-averaged spectral analysis.

In addition to this, for the spectral analysis, we have used the same NaI and BGO detectors and reduced the spectrum using the gtburst software. We selected the total emission interval (T_0 to T_0 +67.38 s) for the time-averaged spectral analysis using a Bayesian block algorithm. For the spectral modelling of both time-averaged as well as time-resolved spectra, we have used the Multi-Mission Maximum Likelihood framework (Vianello et al. 2015, 3ML[3]) software. We selected the GBM spectrum over 8-900 keV and 250-40000 keV for NaI detectors and BGO detector, respectively. In addition, we have ignored the NaI K-edge (30-40 keV) energy range for both
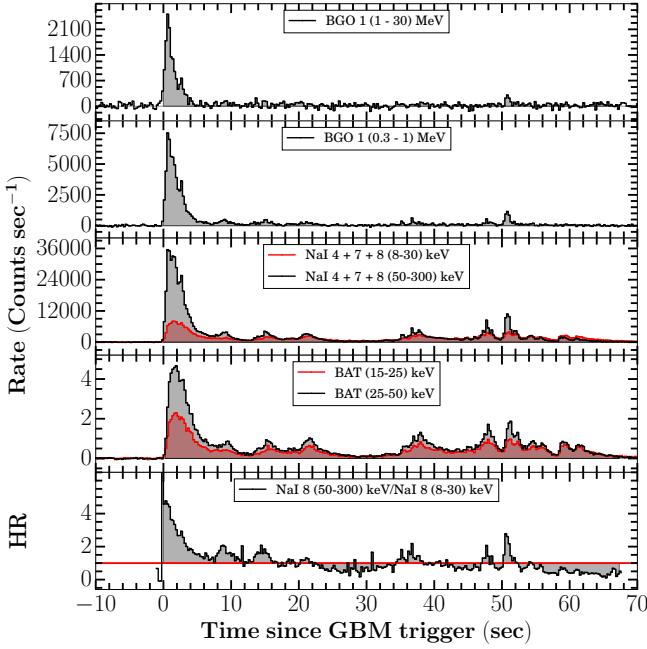

Figure 1. Prompt light curve of GRB 210619B: The top four panels show the background-subtracted multi-channel prompt emission light curve of GRB 210619B obtained using *Fermi* GBM and *Swift* BAT observations (256 ms bin size). The grey and red shading regions show the time-interval (T_0 to $T_0 + 67.38$ s) of the light curve used for the time-averaged spectral analysis. The bottom-most panel shows the hardness ratio, obtained using the ratio of the count-rate light curve in the hard and soft energy range. The solid red line indicates the hardness ratio equal to one.

time-averaged and the time-resolved spectral analysis. For the time-averaged spectral modelling of GRB 210619B, we have used the empirical `Band` function and `Cutoff power-law` models. We adopted the deviation information criterion (DIC; Vianello et al. 2015) to know the best fit function among the `Band`, and `Cutoff power-law` models and selected the best model with the least DIC value (Δ DIC < -10). This suggests that the `Band` function is better fitting with respect to the `Cutoff power-law` model. To know about the best fit model, we utilized the following condition:

$$\Delta DIC = \Delta DIC_{Band} - \Delta DIC_{CPL}$$

The negative values of ΔDIC indicate that there is an improvement in the spectral fit, and if the difference of the deviation information criterion is less than - 10, in such scenario, the existence of `Band` function in the spectrum is confirmed. The time-averaged spectral parameters for both models are tabulated in Table 1.

Time-resolved spectral analysis: We performed the time-resolved spectroscopy of GRB 210619B using the same NaI and BGO detectors used for temporal analysis and the `3ML` software. To select the temporal bins for the time-resolved spectral analysis, we used Bayesian blocks binning algorithm (Scargle et al. 2013). Burgess (2014) suggested that the Bayesian blocks algorithm is crucial to find the finest temporal bins and intrinsic spectral evolution. However, it could result in low signal-to-noise ratio due to high variability in the light curve. Therefore, we further selected only those bins which have statistical significance (S) $\geq$ 30. After implementing the Bayesian blocks and signal-to-noise ratio algorithm, we find a total of 59 spectra for the time-resolved spectroscopy of GRB 210619B (see Table B1 of the appendix). We modelled each

of the time-resolved spectra using individual empirical `Band`, and `Cutoff power-law` models.

2.1.2 ASIM

The Atmosphere-Space Interactions Monitor (ASIM; Neubert et al. 2019) triggered on GRB 210619B on June 19 2021 (Marisaldi et al. 2021). The ASIM reference time used in the rest of the analysis is $T_{0,ASIM}$ = 23:59:24.915550 UT. At trigger time, it was local day time, so only High-Energy Detector (HED) data are available for this event. The burst direction was 135° off-axis with respect to the Modular X- and Gamma-ray Sensor (MXGS; Østgaard et al. 2019) pointing direction. This is outside the instrument's nominal field of view, but the instrument is sensitive to the full solid angle because of its characteristics and high energy range. Photons interaction in the surrounding material and in the Columbus module are accounted for in the Monte Carlo simulation model of the instrument performed using the GEANT4 simulation toolkit (Agostinelli et al. 2003). This model was used to generate the Detector Response Matrix (DRM) of the instrument used for the spectral analysis.

Instrumental effects are carefully accounted for in HED data analysis by the implementation of the "safety time" criterion, described in details in Lindanger et al. (2021). This procedure removes any count which is closer in time to the previous count in the same detector than a specific time interval, ranging from 0 and 30 μs depending on the energy of the previous count. This procedure is introduced to guarantee the best possible energy estimate, which is to some extent affected by the energy of the previous counts. This effect is particularly relevant for **Terrestrial Gamma-ray Flashes (TGFs)**, which exhibit very high fluxes on time scales of few hundreds of microseconds. In the case of GRB 210619B, this effect is almost negligible and the "safety time" criterion removes only about 0.7% of the counts.

The top panel of Figure 2 shows the light curve of ASIM HED data. Because of the characteristics of the ASIM trigger logic, only part of the burst has been collected. A data gap is evident between 4.5 and 8 s after ASIM reference time ($T_{0,ASIM}$). Only limited data are available prior to $T_{0,ASIM}$, therefore the background estimation for spectral analysis is based on the data in the time interval (−420 to 0 ms) with respect to $T_{0,ASIM}$. To assess the spectral evolution of the burst, ASIM HED data were divided into seven-time intervals, as shown in the top panel of Figure 2. The choice of the intervals has been made in order to include in separate intervals all the peaks evident in the light curve (intervals 2, 3, 4, and 5). The spectral fitting has been carried out using `XSPEC` version 12.12. To estimate the flux, the convolution model `cflux` has been used. All time intervals from 1 to 6 can be well fit with a simple power law in the energy range 0.5 to 10 MeV. The best-fit parameters and the fluxes in the energy range 0.5 to 10 MeV are shown in Table 2. The bottom panel of Figure 2 shows the spectra, data points, and best fit models, as well as the residuals for all intervals.

2.1.3 Swift *BAT* and other gamma-ray detectors

The BAT detected GRB 210619B (see the mask-weighted light curve in Figure 1) at 23:59:25 UT on 19 June 2021 at the following location in the sky: RA = 319.713, DEC = +33.860 deg. (J2000) with an error radius of 3 arcmin (D'Avanzo et al. 2021a). The *Swift* BAT and *Fermi* GBM positions were consistent for GRB 210619B.

We downloaded the *Swift* BAT observations data of GRB 210619B

Table 1. The time-averaged (T$_0$ to T$_0$ + 67.38 s) spectral analysis results of GRB 210619B. The best fit model (Band) is highlighted with boldface.

Model	Spectral parameters			-Log(posterior)	DIC	Δ DIC
Band	$\boldsymbol{\alpha_{pt}= -0.90^{+0.01}_{-0.01}}$	$\boldsymbol{\beta_{pt}= -2.05^{+0.02}_{-0.02}}$	$\boldsymbol{E_p = 216.08^{+4.20}_{-4.20}}$	**-4347.76**	**8693.99**	–
CPL	$\alpha_{pt}= -1.03^{+0.01}_{-0.01}$	$E_0 = 320.30^{+5.74}_{-5.63}$		-4633.92	9251.24	-557.25

Table 2. *ASIM* time-resolved spectral analysis results for GRB 210619B. Time intervals have been referred with respect to the ASIM reference time (T$_{0,ASIM}$).

Interval	Time interval (s)	Photon Index	χ^2 (d.o.f.)	Flux (0.5 − 10 MeV) (10^{-5} erg cm^{-2}s^{-1})
1	0.00 − 1.00	$2.11^{+0.12}_{-0.11}$	11.69 (16)	$1.31^{+0.23}_{-0.19}$
2	1.00 − 1.70	$2.25^{+0.03}_{-0.03}$	15.92 (12)	$6.89^{+0.27}_{-0.26}$
3	1.70 − 2.18	$2.49^{+0.06}_{-0.06}$	6.99 (12)	$4.02^{+0.30}_{-0.28}$
4	2.18 − 2.79	$2.60^{+0.09}_{-0.08}$	7.43 (12)	$2.56^{+0.56}_{-0.46}$
5	2.79 − 3.60	$2.56^{+0.11}_{-0.10}$	13.31 (12)	$1.81^{+0.51}_{-0.40}$
6	3.60 − 4.50	$2.97^{+0.37}_{-0.30}$	9.31 (12)	$0.69^{+0.12}_{-0.11}$
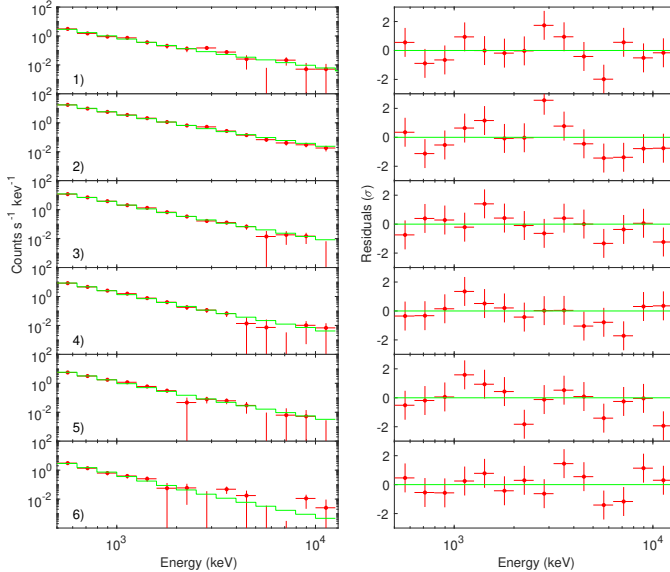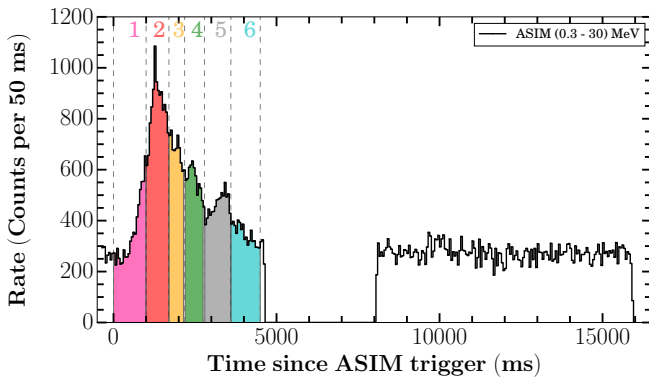
Figure 2. Top panel: The prompt emission (0.3 - 30) MeV light curve of the burst as seen by ASIM/HED. Vertical colored shaded regions (lines) separate the time intervals used for spectral analysis, labeled by numbers on top of the panel. Bottom Left panel: Time-resolved spectra for ASIM data. Data points (red) and best fit power-law model (green). The labels indicate the corresponding time interval. Bottom right panels: residuals of the model fitting.

from the *Swift* database portal[4]. We processed the BAT data using the HEASOFT software (version 6.25). We reduced the *Swift* BAT data following the methodology presented in Gupta et al. (2021) to obtain the energy-resolved mask-weighted light curve. The BAT light curves along with HR evolution in 25-50 keV and 50-100 keV energy range is shown in Figure 1.

The prompt emission of GRB 210619B was also detected by the Gravitational wave high energy Electromagnetic Counterpart All sky Monitor (*GECAM*; Zhao et al. 2021), the *Konus*-Wind Experiment (Svinkin et al. 2021), the *CALET* Gamma-ray Burst Monitor (CGBM; Kawakubo et al. 2021), the Mikhail Pavlinsky ART-XC telescope on board the *Spektr-RG* observatory (Levin et al. 2021), and the SPI-ACS/*INTEGRAL* (Minaev et al. 2021) satellites.

2.1.4 Joint BAT-GBM-ASIM spectral analysis

We performed joint spectral analysis of *Swift* BAT, *Fermi* GBM, and ASIM observations during the main emission pulse of GRB 210619B, using the capabilities of 3ML software [simultaneous spectral fitting of data (even if data does not obey the same likelihoods) observed by different instruments at different energy ranges] to know the radiative processes fueling the bright pulse of GRB 210619B. For this purpose, we created the time-sliced (six bins) spectra using *Swift* BAT and *Fermi* GBM data for the same temporal segments of ASIM (time-resolved analysis) discussed in section 2.1.2 for the joint spectral analysis. We obtained the continuous spectra in the overlapping energy regions of *Swift* BAT (15-150 keV), *Fermi* GBM (8 keV-40 MeV), and ASIM (500 keV to 10 MeV) instruments. We have used the same models and statistics for the joint spectral analysis, which we used for *Fermi* GBM spectral analysis (see section 2.1.1). We applied the effective area correction between the *Swift* BAT, *Fermi* GBM, and ASIM detectors to model systematic problems in detectors calibration. Effective area corrections allow to vary the normalization and scale the counts of detectors by a multiplicative factor to obtain the calibration. The joint *Swift* BAT, *Fermi* GBM, and ASIM count rate spectrum along with the best fit model and residuals for one of the time bins (T$_{0,ASIM}$+1.00 to T$_{0,ASIM}$+ 1.70 s) is shown in Figure 3 and the corresponding corner plot is shown in Figure B1 of the appendix. The spectral parameters for all the six bins are given in Table B2 of the appendix. We note that

---

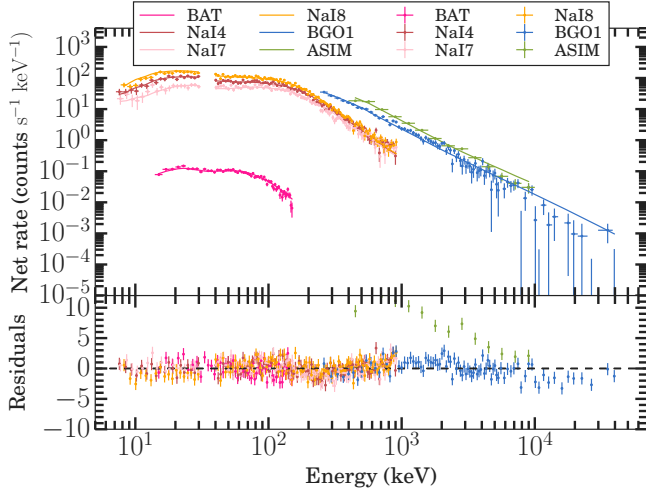[4] https://www.swift.ac.uk/swift_portal/

Figure 3. Top panel: The best fit (Band) joint *Swift* BAT (15-150 keV), *Fermi* GBM (8 keV-40 MeV), and ASIM (500 keV to 10 MeV) spectrum for the temporal bin 2 ($T_{0,ASIM}$+1.00 to $T_{0,ASIM}$+ 1.70 s) of GRB 210619B. Bottom panel: The corresponding residuals of the model fitting.

all the joint BAT-GBM-ASIM spectra are well fitted using Band function.

2.2 Results

The prompt emission results of GRB 210619B obtained using *Fermi* and ASIM data are presented in this section.

2.2.1 Light curve and time-integrated spectrum

The prompt *Fermi* GBM and *Swift* BAT light curve of GRB 210619B consists of a very bright main pulse followed by a long fainter emission activities up to ∼ 70 s post trigger time. On the other hand, ASIM observed only the main bright pulse, displaying a Fast-Rise Exponential Decay (FRED) type structure (see Figure 2). Based on the DIC condition given in section 2.1.1, we find that the time-averaged spectra (T_0 to T_0 +67.38 s) of GRB 210619B **in the energy range from 8 keV to 40 MeV** could be best fitted using the Band model. We obtained the following best fit spectral parameters: α_{pt}= -0.90$^{+0.01}_{-0.01}$, β_{pt}= -2.05$^{+0.02}_{-0.02}$, and the spectral peak energy E_p = 216.08$^{+4.20}_{-4.20}$ keV. The best fit time-averaged spectrum of GRB 210619B along with the corresponding corner plot is shown in Figure 4.

2.2.2 Empirical correlations: Amati and Yonetoku

The prompt properties of GRBs follow a few global correlations. These correlations are also used characterizing and classifying them into long and short bursts (Minaev & Pozanenko 2020). For example, the time-integrated spectral peak energy (in the source frame) of the burst is positively correlated with the isotropic equivalent gamma-ray energy ($E_{\gamma,iso}$), known as Amati correlation (Amati 2006). We calculated $E_{\gamma,iso}$ and restframe peak energy for GRB 210619B using the best fit time-integrated model parameters and compared the results with a larger sample of GRBs. For the time-integrated interval, we calculated the energy flux equal to 6.27×10^{-6} erg cm^{-2} s^{-1} in the source frame (0.34 keV to 3404.8 keV) which is equivalent to $E_{\gamma,iso}$=
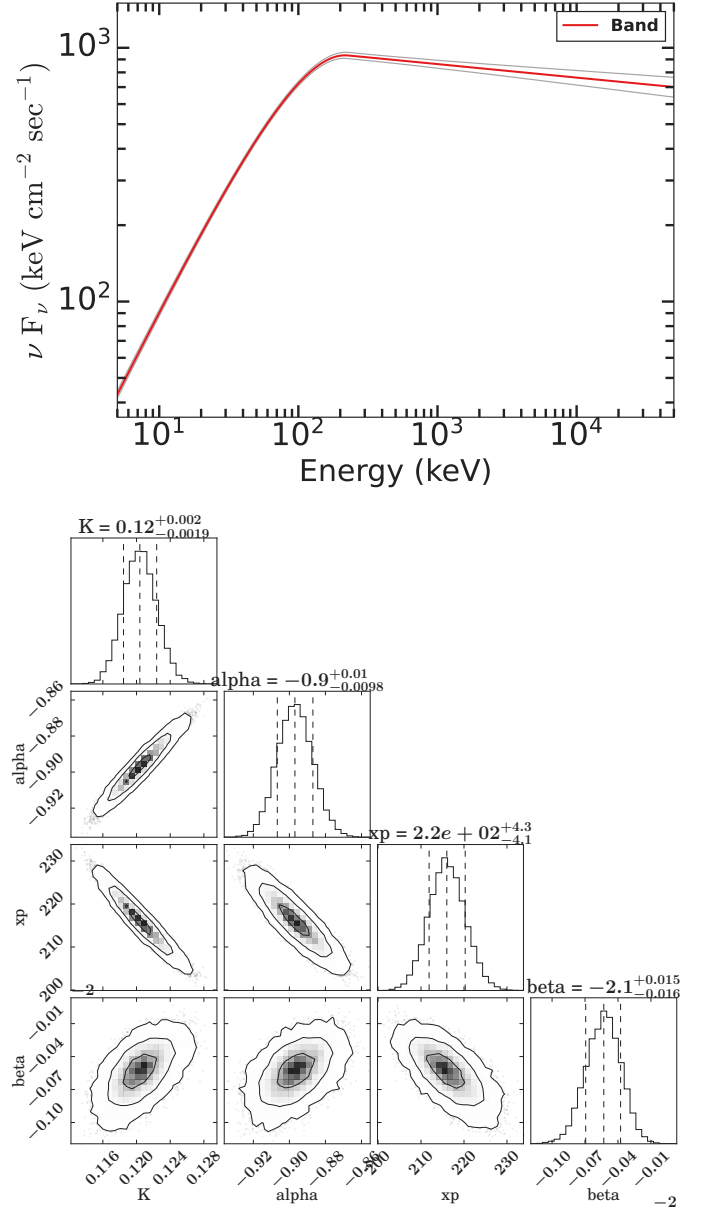

Figure 4. Top panel: The best fit time-averaged (T_0 to T_0 + 67.38 s) spectrum (Band) of GRB 210619B in model space. The white shaded regions denote the 2 σ uncertainty regions associated with the spectral model parameters. Bottom panel: The corresponding corner plot for 5000 number of simulations.

4.05×10^{54}erg. The $E_{p,z}$-$E_{\gamma,iso}$ correlation for GRB 210619B along with other data points taken from Minaev & Pozanenko (2020) are shown in Figure 5. GRB 210619B is one of the brightest bursts ever detected by *Fermi* GBM and marginally satisfies the Amati correlation. Furthermore, we also placed GRB 210619B in the $E_{\gamma,iso}$ and redshift distribution plane. The comparison with other well-studied samples (Minaev & Pozanenko 2020; Sharma et al. 2021) indicates that GRB 210619B is one of the brightest bursts at its measured redshift.

Similarly, the time-integrated peak energy (in the source frame) of the burst is also correlated with the isotropic gamma-ray luminosity $L_{\gamma,iso}$, known as Yonetoku correlation (Yonetoku et al. 2010). We modelled the peak spectrum (T_0 +0.50 s to T_0 +1.01 s; see Figure 6)
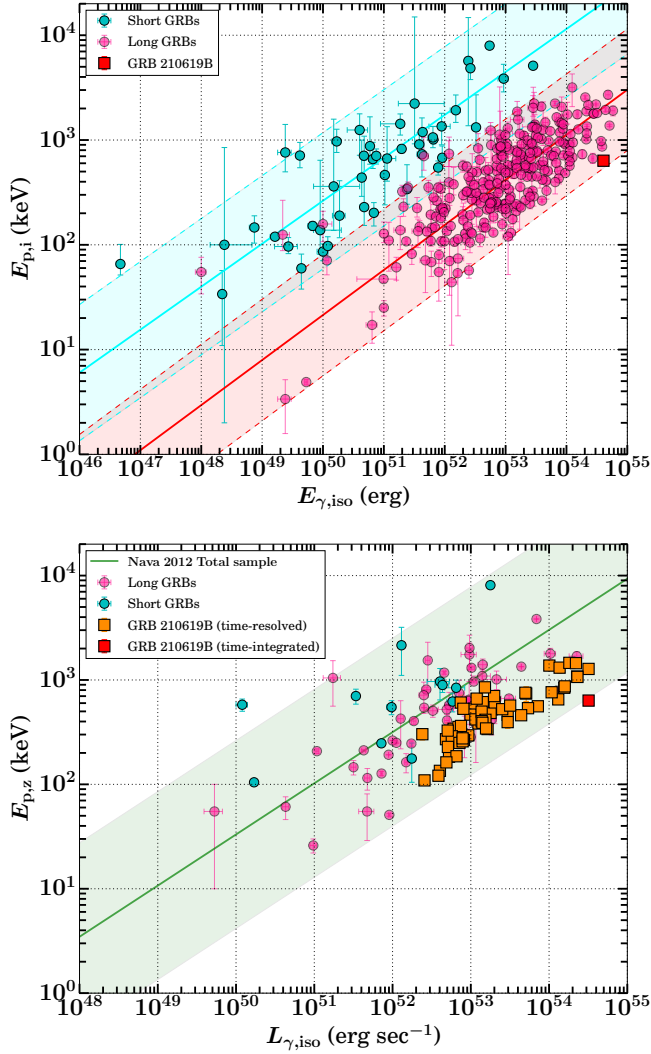
Figure 5. Top panel: GRB 210619B in Amati correlation plane (marked with a red square). The cyan and pink circles denote the long and short GRBs taken from Minaev & Pozanenko (2020). The solid cyan and pink lines show the linear fit lines for short and long GRBs, respectively. The parallel shaded regions show the 3σ scatter of the correlations. Bottom panel: GRB 210619B in Yonetoku correlation plane (marked with a red square for the time-integrated duration and marked with orange squares for each of 59 spectra obtained using the time-resolved Bayesian bins with statistical significance ≥ 30). The cyan and pink circles denote the long and short GRBs taken from Nava et al. (2012). The parallel shaded regions show the 3σ scatter of the correlations.
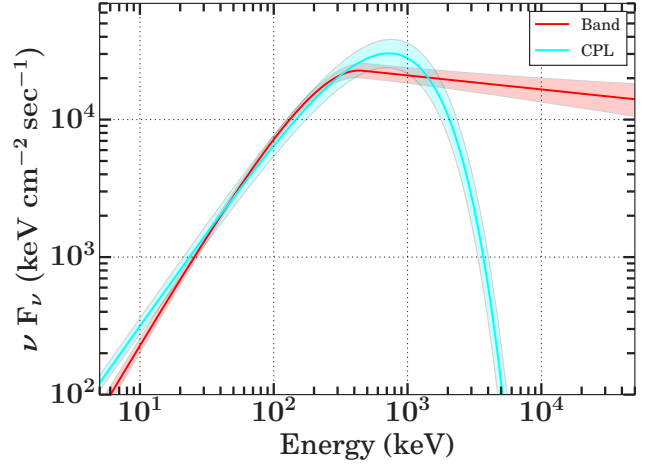

Figure 6. The comparison between different empirical models (the Band function shown in red, and the CPL function shown in cyan) used to fit the peak spectra (**time-interval from** $T_0 +0.50$ s to $T_0 + 1.01$ s**, and energy range from 8** keV **to 40 MeV**) of GRB 210619B in model space. The corresponding shaded colors show the 95 % confidence levels.

used for the time-resolved spectral analysis. Figure 5 shows the time-resolved $E_{p,z}$-$L_{\gamma,iso}$ correlation for GRB 210619B. We noticed that the time-resolved Yonetoku correlation for GRB 210619B is well consistent with that from the time-integrated Yonetoku correlation studied by Nava et al. (2012).

2.2.3 T_{90}-hardness distribution

GRBs are mainly classified based on the prompt emission properties such as T_{90} duration and hardness ratio. Long duration GRBs have a softer spectrum in contrast to short duration GRBs; therefore, long and short GRBs are positioned at different places in the T_{90}-hardness distribution plane of GRBs. We collected the T_{90} duration and peak energy values of all the bursts detected by *Fermi* GBM from the GBM burst catalog[5] (Gruber et al. 2014; Bhat et al. 2016; Von Kienlin et al. 2020). The time-integrated T_{90}-hardness distribution for *Fermi* GBM detected GRBs is shown in Figure 7. The position of GRB 210619B is shown with a red square, and GRB 210619B follows the distribution of long GRBs. Furthermore, we also calculated the time-integrated hardness ratio (HR) by taking the ratio of counts in hard (50-300 keV) and soft (10-50 keV) energy channels. We find HR= 1.16 for GRB 210619B. Figure 7 shows the T_{90}-HR distribution for GRB 210619B along with other long and short duration GRBs taken from Goldstein et al. (2017).

2.2.4 T_{90}-Minimum variability time

The prompt emission light curve of GRBs is variable in nature due to being originated from internal shocks (Pe'er 2015). The minimum variability time for long (less variable) and short (more variable) GRBs follows a different distribution due to diverse compact central sources. The minimum time variability timescale, t_{mvts}, is useful to constrain the minimum value of the bulk Lorentz factor

of GRB 210619B to calculate the $L_{\gamma,iso}$. For the peak time-interval, we calculated the energy flux equal to 1.14×10^{-4}erg cm^{-2} s^{-1} in the source frame (0.34 keV to 3404.8 keV) and it is equivalent to $L_{\gamma,iso}=$ 3.20×10^{54}erg s^{-1}. The Yonetoku correlation for GRB 210619B along with other data points taken from Nava et al. (2012) are shown in Figure 5. GRB 210619B is one of the most luminous bursts ever detected by *Fermi* GBM and marginally satisfied the Yonetoku correlation. In addition to time-integrated $E_{p,z}$-$L_{\gamma,iso}$ correlation, we also examined the time-resolved $E_{p,z}$-$L_{\gamma,iso}$ relation for GRB 210619B. For this purpose, we calculated the $L_{\gamma,iso}$ values for each (a total of 59 spectra) of the Bayesian bins with statistical significance (S) ≥ 30

---

[5] https://heasarc.gsfc.nasa.gov/W3Browse/fermi/fermigbrst.html

We calculated the minimum value of the bulk Lorentz factor and the emission radius, giving $\gtrsim 550$ and $\simeq 1.87 \times 10^{15}$ cm respectively, for GRB 210619B. We also calculated the bulk Lorentz factor value ($\Gamma = 817$) for GRB 210619B using the Γ_0-$E_{\gamma,\text{iso}}$[7] correlation (Liang et al. 2010) and noticed that the minimum value of the bulk Lorentz factor constrained using the minimum variability time scale is consistent with the value of the Lorentz factor found using the correlation. **The calculated radius for GRB 210619B is much larger than the typical emission radius of the photosphere, indicating that the emission took place in an optically thin region away from the central engine (Uhm & Zhang 2016; Ravasio et al. 2019; Burgess et al. 2020).**

2.2.5 Spectral lag

The prompt emission light curves of long GRBs (short GRBs) show significant (zero) delays in two different energy ranges, and this characteristic is known as spectral lag. If the high-energy photons of GRBs come before the low-energy photons, it is defined as positive spectral lag. On the other hand, we conventionally defined the lag as negative if the low-energy photons precede the high-energy photons. The observed spectral lag is usually explained in terms of the prompt intrinsic spectral evolution (mainly temporal evolution of E_p) or due to the curvature effect of relativistic moving shocked shells (Dermer 2004; Uhm & Zhang 2016). Norris et al. (2000) reported the anti-correlation between the spectral lag and isotropic peak luminosity of GRBs using a limited long bursts sample (with known redshift) observed using the *BATSE* mission.

In the case of GRB 210619B, we initially estimated the time-integrated (T_0 to T_0 +67.38 s) spectral/timing lag for the *Swift* BAT light curves (see Figure 8) in two different energy ranges (15-25 keV and 50-100 keV) using the cross-correlation function (CCF; Norris et al. 2000). We followed the detailed methodology presented in Bernardini et al. (2015). We have used emcee package (Foreman-Mackey et al. 2013) to fit the cross-correlation function using an asymmetric Gaussian function. We obtained a negative spectral lag = -160^{+67}_{-66} ms and placed it in the anti-correlation relationship between the spectral lag and isotropic peak luminosity of GRBs (data taken from Ukwatta et al. 2010 in the same energy range). We noticed that GRB 210619B is an outlier of the lag-luminosity anti-correlation relationship (see middle panel of Figure 8). Furthermore, we examined the literature and found that many long GRBs (GRB 060814, GRB 061021, GRB 070306, GRB 080721, GRB 080804, GRB 090426C, GRB 100728B, GRB 110205A, GRB 140102A, GRB 150213A, and many others) are reported with such a large value (> -100 ms, although with large error bars) for the negative spectral lag (Bernardini et al. 2015; Chakrabarti et al. 2018; Gupta et al. 2021). Bernardini et al. (2015) studied a larger sample of long and short GRBs and noticed that the bursts with high luminosity might have smaller lags. Minaev et al. (2014) proposed that the GRBs independent emission pulses exhibit hard-to-soft spectral evolution of the peak energy, suggesting a positive spectral lag (Uhm et al. 2018). However, a strong/complex spectral evolution of peak energy could result in superposition effects, and this superposition effect could explain the negative spectral lag observed for GRB 210619B.

In addition, we also performed the energy-resolved spectral lag analysis (T_0 to T_0 +67.38 s) of GRB 210619B using *Swift* BAT and *Fermi* GBM observations. We considered the 15-25 keV and 8-30 keV light curves as reference to calculate the lag using *Swift* BAT
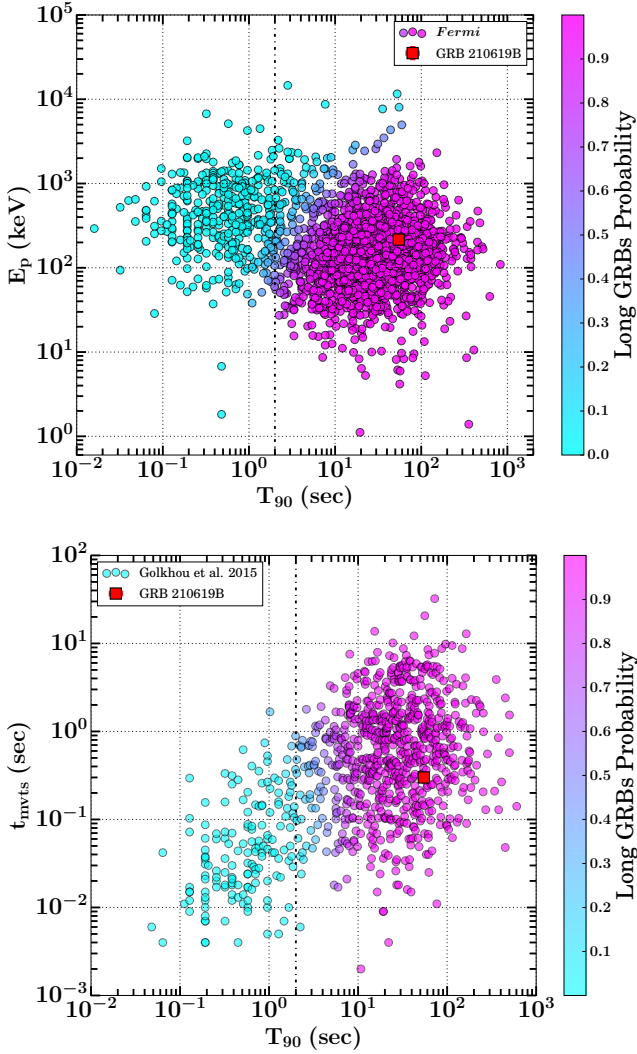

Figure 7. Top panel: Spectral peak energy as a function of T_{90} duration for GRB 210619B along with all the bursts detected by *Fermi* GBM. Bottom panel: Minimum variability time scale as a function of T_{90} duration for GRB 210619B along with other long and short duration GRBs taken from Golkhou et al. (2015). The right side color bar (Y-scale) shows the probability of long GRBs in respective plots. The vertical dashed-dotted black line denotes the boundary of two GRBs families.

(Γ_{min}) and the emission radius (R_c). We calculated the t_{mvts} (~ 0.3 s) for GRB 210619B following the continuous wavelet transforms[6] methodology given in Vianello et al. (2018). The T_{90}-t_{mvts} distribution for long and short GRBs (taken from Golkhou et al. 2015) along with GRB 210619B are shown in Figure 7 (bottom panel).

Furthermore, we estimated Γ_{min} and R_c using the following equations from Golkhou et al. (2015):

$$\Gamma_{\text{min}} \gtrsim 110 \left(\frac{L_{\gamma,\text{iso}}}{10^{51} \text{ erg/s}} \frac{1+z}{t_{\text{mvts}}/0.1 \text{ s}} \right)^{1/5} \tag{1}$$

$$R_c \simeq 7.3 \times 10^{13} \left(\frac{L_{\gamma,\text{iso}}}{10^{51} \text{ erg/s}} \right)^{2/5} \left(\frac{t_{\text{mvts}}/0.1 \text{ s}}{1+z} \right)^{3/5} \text{ cm.} \tag{2}$$

---

[6] https://github.com/giacomov/mvts

[7] $\Gamma_0 \approx 182 \times E_{\gamma,\text{iso},52}^{0.25 \pm 0.03}$

Figure 9. The difference between DIC values of `Band` and `Cutoff-power law` models for each of the time-resolved bins obtained using Bayesian block analysis (with S ≥ 30). The horizontal red dashed, and solid red lines show the difference between DIC values equal zero and -10, respectively.

and *Fermi* GBM respectively. We noticed that the energy-resolved lag analysis also shows the negative lag, suggesting that the low-energy photons precede the high-energy photons for GRB 210619B. Figure 8 (bottom panel) shows the spectral evolution of the lags for GRB 210619B. The energy-resolved spectral lags obtained using BAT, and GBM data are tabulated in Table B3 of the appendix.

2.2.6 Spectral Evolution and correlations

The prompt emission is believed to consist of various spectral components, the combination of which provides the shape of the observed spectrum. To constrain these components for GRB 210619B, we performed the time-resolved spectral analysis (see section 2.1.1). Figure 9 shows the difference of deviation information criterion values from `Band` and `Cutoff-power law` functions for each of the time-resolved bins (a total of 59 bins) obtained using Bayesian block analysis with S ≥ 30. The comparison of differences of the DIC values for each bin suggests that most of the bins (except five) support the traditional `Band` model. Figure 10 shows the distribution of spectral parameters (E_p, α_{pt}, β_{pt}, and flux) obtained using the `Band` model. We have also shown the kernel density estimation (KDE) for each of the parameters. The averaged and standard deviation values of individual spectral parameter distributions are given in Table 3.

The prompt emission spectral parameters of GRBs exhibit a strong spectral evolution and are useful to understand the radiation mechanisms and jet composition of GRBs. Figure 11 shows the evolution of spectral parameters (E_p, α_{pt}, β_{pt}, and flux) for GRB 210619B obtained using the the `Band` model. In the Figure, the evolution of spectral parameters is over-plotted on the count-rate prompt emission light curve of GRB 210619B. We noticed that the evolution of observed E_p exhibits an intensity tracking pattern for GRB 210619B. The observed negative spectral lag (see section 2.2.5) and intensity tracking behaviour of E_p for GRB 210619B is consistent with the prediction of a connection between the spectral lag and spectral evolution (Uhm et al. 2018). Moreover, the low-energy index also
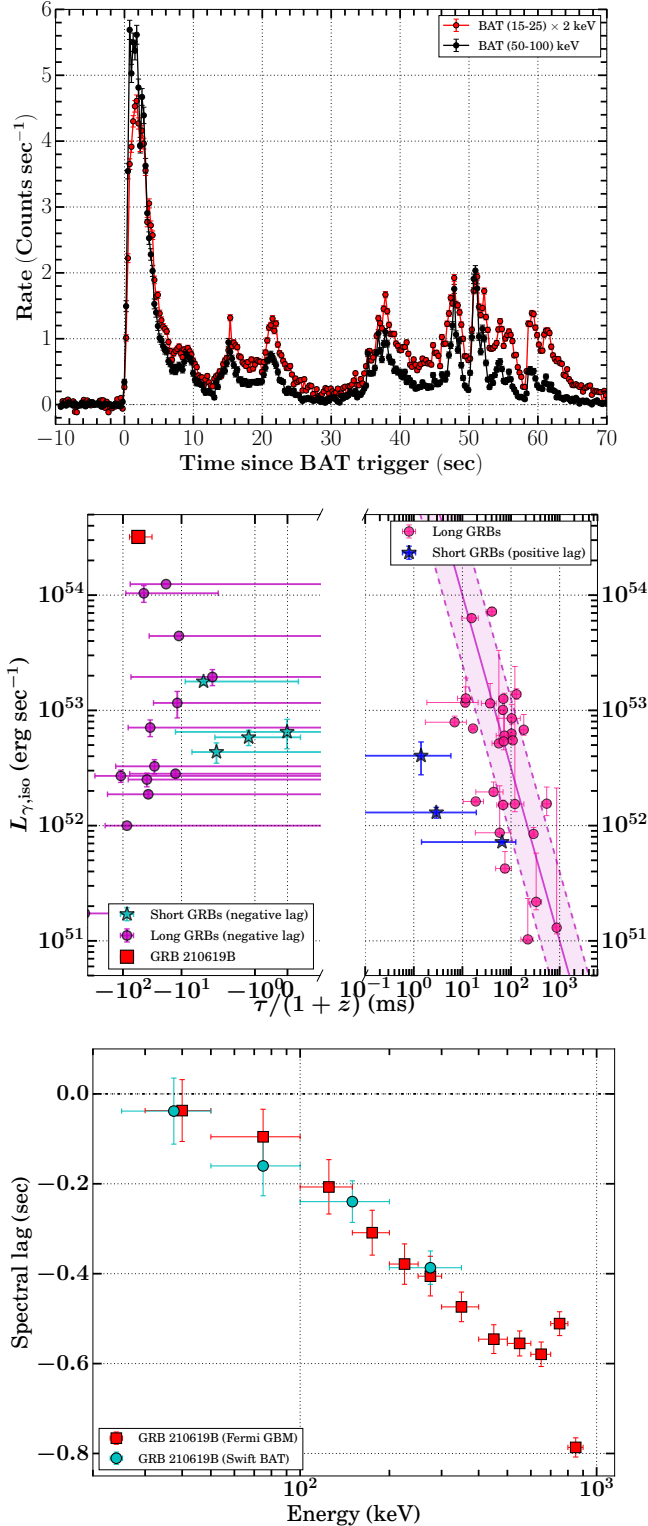
Figure 8. Spectral lag of GRB 210619B: Top panel: *Swift* BAT count rate light curves in 15-25 keV (shown with red) and 50-100 keV (shown with black) energy range, with bin size of 256 ms. Middle panel: Lag-luminosity correlation for GRB 210619B in *Swift* BAT 50-100 keV and 15-25 keV energy ranges along with other data points taken from Ukwatta et al. (2010); Bernardini et al. (2015). Bottom panel: Energy-resolved spectral lag analysis of GRB 210619B using *Swift* BAT and *Fermi* GBM observations.
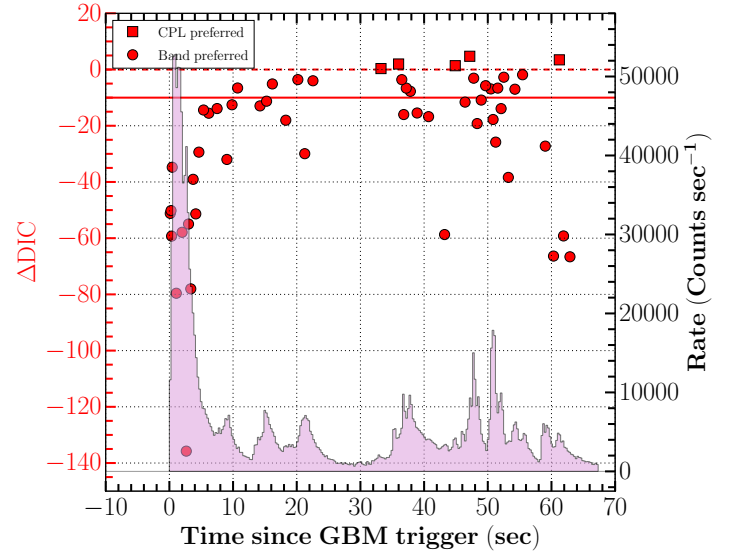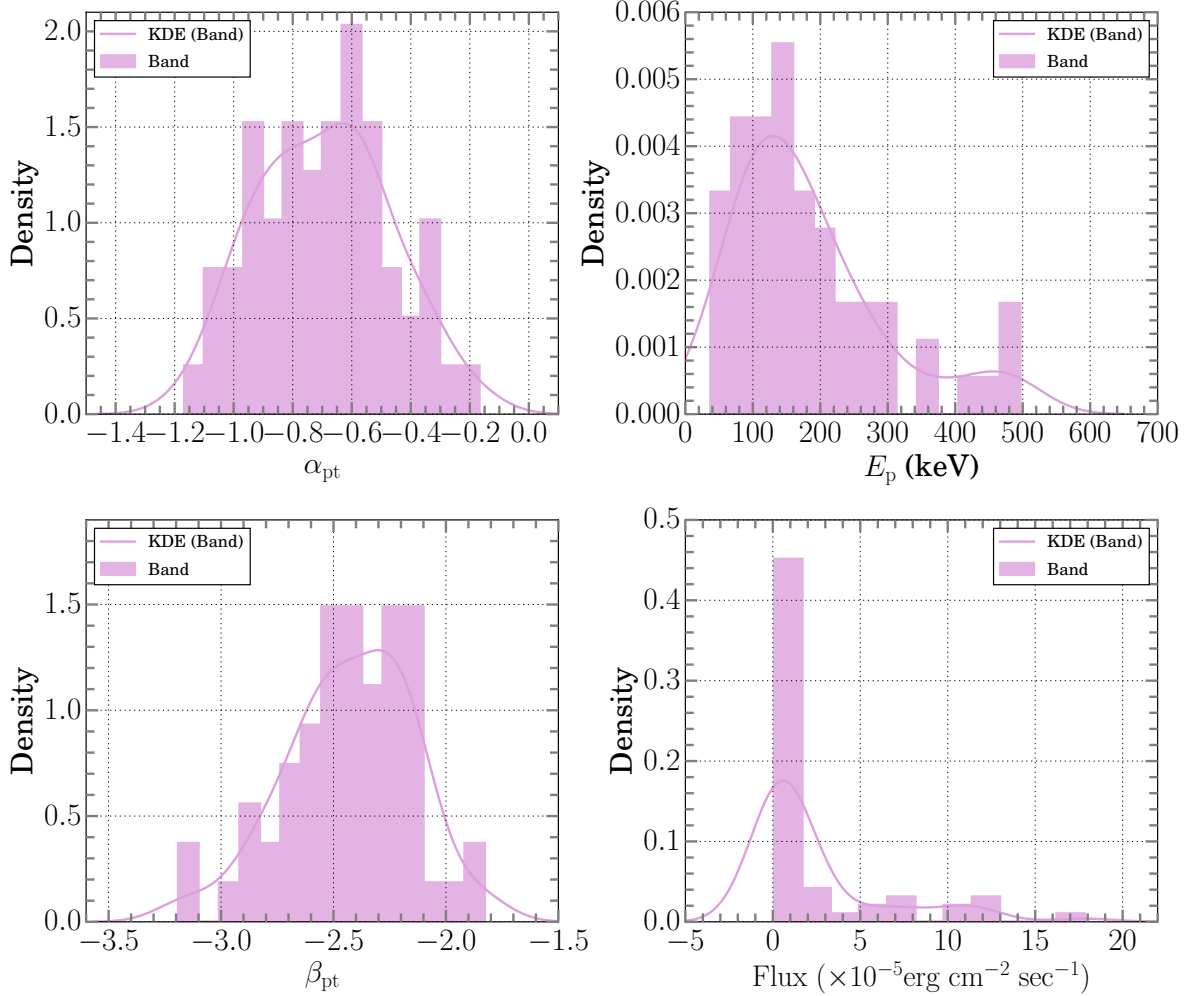
Table 3. The averaged and standard deviation of individual spectral parameters distributions for GRB 210619B.

Model	Spectral parameters			
	α_{pt}	E_p/E_c (keV)	β_{pt}	Flux ($\times 10^{-05}$ erg s^{-1})
Band	-0.69 ± 0.22	183.47 ± 113.90	-2.43 ± 0.28	2.37 ± 3.88
CPL	-0.88 ± 0.20	214.52 ± 128.63	-	1.45 ± 2.34

Figure 10. The spectral parameters (α_{pt}, E_p, β_{pt}, and flux) distributions for GRB 210619B obtained using the time-resolved spectral analysis of *Fermi* GBM data using the Band model. The plum curves show the kernel density estimation (KDE) of the respective parameters distributions fitted using the Band model.

exhibits an intensity tracking trend, suggesting the double-tracking characteristics seen in a few cases of GRBs. Further, we examined the overall spectral parameters correlations.

We studied the correlation between the following spectral parameters: (a) log (Flux)-log (E_p), (b) log (Flux)-α_{pt}, and (c) log (E_p)-α_{pt}. We have utilized Pearson correlation to calculate the correlation strengths (Pearson correlation coefficient, r) and the probability of a null hypothesis (p) for individual parameters correlation. We noticed a strong correlation for both (a) log (Flux)-log (E_p), and (b) log (Flux)-α_{pt}. On the other hand, log (E_p)-α_{pt} shows a moderate degree of correlation (see Table 4). Figure 12 shows the correlation between the spectral parameters obtained using the time-resolved spectral modelling with the Band model. The time-resolved spectral analysis (using ASIM data) of the main bright pulse observed with ASIM shows evidence for hard-to-soft spectral evolution (softening when

brightening behaviour), which is significant at 95% confidence level for the first two (three) time intervals (see Table 2). This characteristic is consistent with *Fermi* time-resolved spectral analysis results during the main bright pulse; therefore it shows agreement between the two observations.

2.3 Discussion

Based on the above mentioned results using the **high energy** analysis of the prompt emission properties of GRB 210619B, our major findings are discussed below in the following sub-sections.

Table 4. The correlation between the spectral parameters obtained using the time-resolved spectral analysis of GRB 210619B. We have used Pearson correlation to calculate the correlation strengths (Pearson correlation coefficient, r) and the probability of null hypothesis (p) for individual parameters correlation.

Model	log (Flux)-log (E_p)		log (Flux)-α_{pt}		log (E_p)-α_{pt}	
	r	**p**	**r**	**p**	**r**	**p**
Band	0.87	2.07×10^{-19}	0.75	1.10×10^{-11}	0.47	1.85×10^{-4}
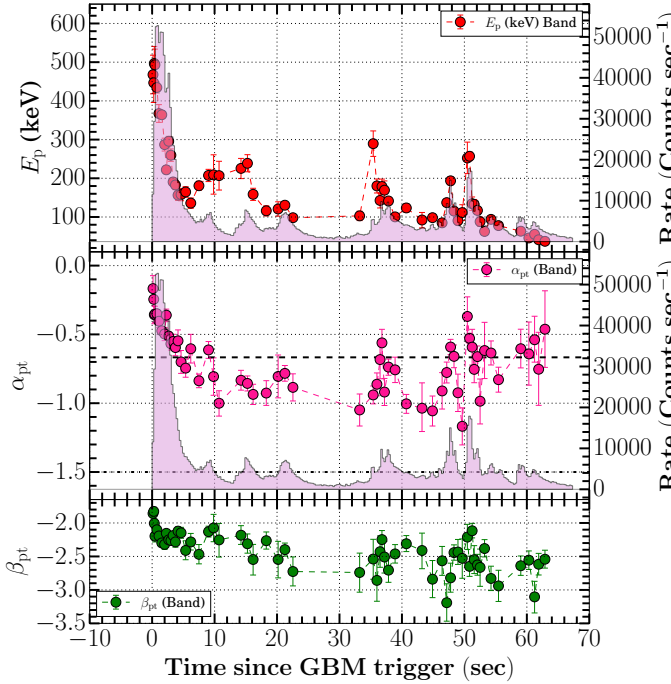
Figure 11. Temporal evolution of spectral parameters obtained using time-resolved spectral modelling with the Band model: Top panel: Evolution of peak energy and it tracks the intensity of the burst. Medium panel: Evolution of low-energy spectral index. The horizontal dashed and dotted-dashed lines represent the synchrotron line of death (α_{pt} = -2/3) and the synchrotron fast cooling line (α_{pt} = -3/2). Bottom panel: Evolution of high-energy spectral index obtained using the Band spectral model.

2.3.1 Prompt emission mechanism and jet composition

Regarding the observed prompt emission, the spectrum was explored to find the possible radiation mechanism of GRBs. There are mainly two possibilities, non-thermal thin shell synchrotron emission or photospheric thermal emission (Pe'er 2015; Zhang 2020). The non-thermal thin shell synchrotron emission suggests that the low-energy photon indices could not be harder than the -2/3 value, also known as "synchrotron line of death (LOD)". However, in the case of GRB 210619B, the evolution of the low-energy photon indices exceeds the synchrotron LOD during the main bright/hard pulse, and during the softer/longer pulses, the low-energy photon indices become softer and remain consistent with this limit (see Figure 11). The observed hard values of the low-energy photon indices (during the main pulse emission) suggest that the observed prompt emission spectrum of GRB 210619B is inconsistent with the non-thermal thin shell synchrotron emission model (both in slow and fast cooling cases). This hard α_{pt} also suggests that our viewing angle for the burst is not significantly off the burst emission axis and that the central engine has been long-time active. The hard α_{pt} could be explained using thermal "photospheric emission" (Pe'er 2015; Iyyani

2018). On the other hand, the softer values of the low-energy photon indices during the longer emission phase are consistent with the non-thermal thin shell synchrotron emission model. This suggests that the radiation process responsible for GRB 210619B shows a transition between photospheric thermal emission (hard α_{pt}) and non-thermal synchrotron emission (soft α_{pt}). This further supports a transition in the jet composition of GRB 210619B, between a matter-dominated hot fireball (Usov 1992; Pe'er 2015) to Poynting flux dominated outflow (Mészáros & Rees 1997; Lyutikov & Blackman 2001). Such a transition has been observed only for a few bursts (Zhang et al. 2018; Li 2019).

2.3.2 Comparison of spectral parameters with a larger sample

We collected the spectral parameters of single and multi-episodic bursts and compared them with those of GRB 210619B. Figure 13 (top panel) shows the distribution of time-resolved peak energy as a function of energy flux of GRB 210619B along with a large sample of GRBs. We noticed that the mean values of energy flux from GRB 210619B are significantly larger than the mean value of similar multi-pulsed GRBs; however, the mean values of the peak energy from GRB 210619B are softer in comparison with the mean values of multi-pulsed GRBs. Figure 13 (middle panel) shows the distribution of time-resolved low-energy photon indices as a function of energy flux of GRB 210619B along with a large sample of GRBs. The α_{pt} values of GRB 210619B exceed the synchrotron LOD during the brighter phase. We also found that for some of the single and multi-pulsed GRBs even exceed the low-energy photon index, predicted from jitter radiation (α_{pt} = +0.5; Medvedev 2000). Figure 13 (bottom panel) shows the distribution of time-resolved peak energy as a function of α_{pt} of GRB 210619B along with a large sample of GRBs. Furthermore, we also compared the spectral parameters of GRB 210619B with those bursts (GRB 131231A, GRB 140102A, GRB 190530A, and others) having "Double-tracking" evolution pattern of E_p and α_{pt} (Li et al. 2019; Gupta et al. 2021, 2022). We noticed that some bursts are consistent with the non-thermal thin shell synchrotron emission model, however, some of them required a hybrid non-thermal synchrotron plus thermal photospheric emission. This suggests that the observed "Double-tracking" evolution characteristics could be independent of the emission mechanisms of GRBs, though many more such bright bursts are needed to be analysed and physically modelled to confirm this.

3 BROADBAND AFTERGLOW EMISSION OF GRB 210619B

3.1 Observations and data analysis

Followed by the *Fermi* and *Swift* detection of GRB 210619B with larger error circles; further localization improvements were made with the X-ray Telescope (XRT) and the optical-UV telescope (UVOT) on-board *Swift* (Beardmore et al. 2021; Page et al. 2021). This triggered several facilities on-ground and further in space. This section presents the **broadband afterglow** observational **, and data**
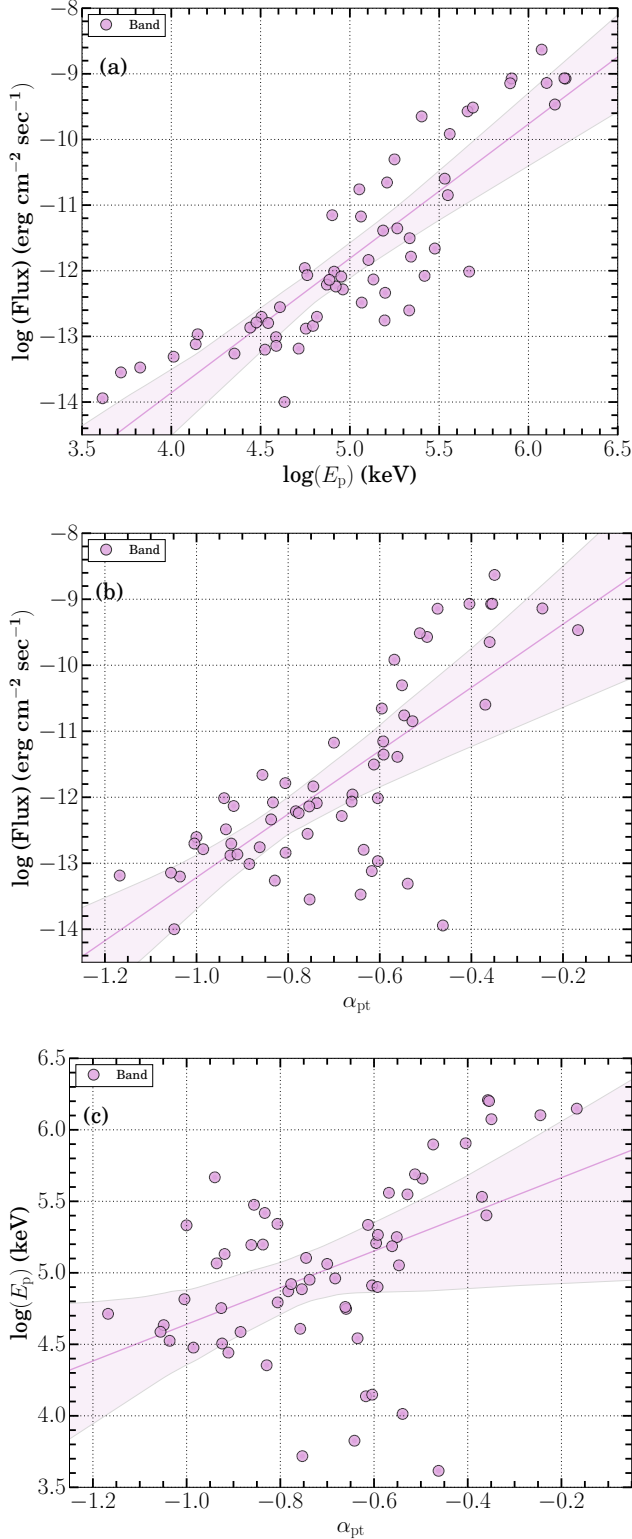
Figure 12. Correlation between the spectral parameters obtained using time-resolved spectral modelling with the Band model: (a) Correlation between the peak energy and flux. (b) Correlation between the low-energy spectral index and flux. (c) Correlation between the peak energy and the low-energy spectral index.
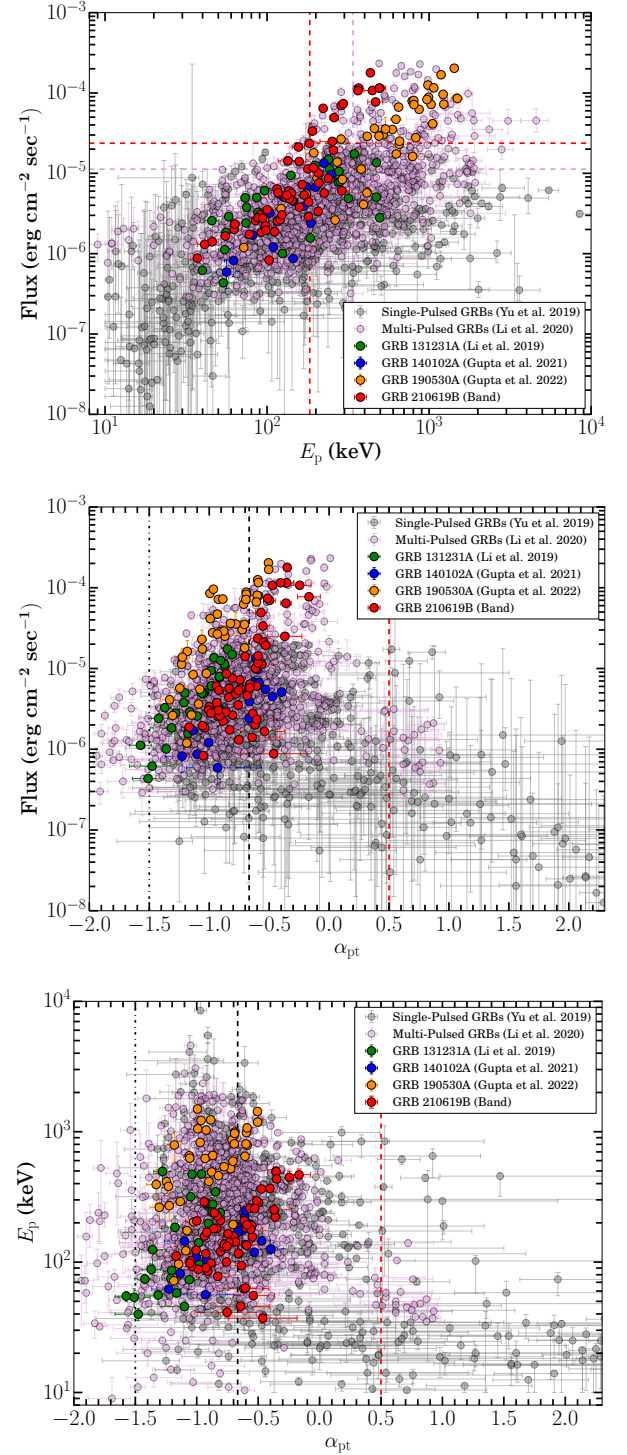

Figure 13. Comparison between the spectral parameters: Top panel: Comparison between the peak energy and energy flux obtained using time-resolved spectral modelling with the Band model for GRB 210619B with well-studied sample of single, multi-pulsed, and Double tracking bursts. The vertical/horizontal pink and plum lines show the mean values of $E_{\rm p}$/flux of GRB 210619B and sample of multi-pulsed GRBs, respectively. Middle panel: Comparison between the low-energy power-law index and energy flux. Bottom panel: Comparison between the low energy power-law index and peak energy. The vertical black dotted-dashed, black dashed, and red dashed lines shows the synchrotron fast cooling, slow cooling, and jitter radiation.

analysis details carried out by our optical follow-up programs using various ground-based telescopes, including the 10.4 m GTC.

3.1.1 Fermi *LAT*

At the *Fermi* GBM trigger time, the burst was outside the *Fermi* Large Area Telescope (LAT) FoV (the boresight angle was 109 deg.) and it came into the FoV $\sim$ 200 s post GBM trigger time. *Fermi* LAT detected high energy emission associated from GRB 210619B at the position RA= 319.7, DEC = 33.9 deg. (J2000) with an error radius of 0.13 deg. (Axelsson et al. 2021).

We extracted the LAT high energy data of GRB 210619B for a time interval of $\sim$ 10 ks (from T_0 +285 s to T_0 +10 ks) using the LAT data server web-page [8] and performed the unbinned likelihood analysis using the official LAT data analysis GUI (python) based software known as `gtburst` [9]. After downloading the LAT data, we used the `Make navigation plots` tool to check when the source was within the FoV of the instrument. We noticed that the source was outside the FoV (source off-axis angle 65°) at the time of T_0. It comes within the FoV at $\sim$ 285 s post *Fermi* trigger and remains till $\sim$ 2850 s post T_0. *Fermi* LAT observed the source multiple times between T_0 +285 s to T_0 +10 ks. For the unbinned likelihood analysis of LAT data, we have used the following parameters: region of interest (ROI) = $10°$, energy range = 100 MeV - 100 GeV, and angular cut = $105°$. For the total time intervals, the source (`P8R3_SOURCE_V2`) response has been used as the data class, and for short temporal bins, we used the transient (`P8R2_TRANSIENT020E_V6`) response. Further, we estimated the probability of the LAT photons being associated with the source using the `gtsrcprob` tool. A more detailed methodology for *Fermi* LAT data analysis is presented in Gupta et al. (2021). We also compared the characteristics of LAT detected GRB 210619B with *Fermi* LAT second GRB catalog (see § 3.2.3).

3.1.2 Swift *XRT*

The soft X-ray observations of GRB 210619B were started by the *Swift* X-ray Telescope (XRT; Burrows et al. 2005) in search of the X-ray afterglow at 00:04:53.4 UT on 20 June 2021 ($\sim$ 328.1 s post *Swift* BAT detection). The XRT discovered a bright and fading uncatalogued X-ray source at the position RA= 319.7161, DEC= 33.8495 deg. (J2000) with an error radius of 11.1 arcseconds (D'Avanzo et al. 2021a). This position was within the *Swift* BAT uncertainty region, 38 arcseconds from the *Swift* BAT onboard location. We obtained the *Swift* XRT temporal and spectral data for the X-ray afterglow of GRB 210619B from the *Swift* XRT GRB lightcurve repository[10] and *Swift* XRT GRB spectrum repository[11], respectively. These repositories are provided by UK Swift Science Data Centre and web pages (Evans et al. 2007, 2009). For the spectral analysis of *Swift* XRT data, we have used the X-ray Spectral Fitting Package (`XSPEC`; Arnaud 1996) software. We have used the XRT spectrum in the 0.3-10 keV energy range and fitted the spectrum using an absorbed power-law model (one model with absorption fixed to the contribution of our Galaxy `phabs` and another with free absorption to constrain this parameter from the contribution of the host galaxy `zphabs`).

3.1.3 BOOTES

The Burst Observer and Optical Transient Exploring System (BOOTES) followed the GRB 210619B trigger with the 60 cm BOOTES-4/MET robotic telescope located at Lijiang Astronomical Observatory, China (Castro-Tirado et al. 2012). The observation was performed on 20 June 2021 at 14:20:16 UT, which is $\sim$ 0.6 day after the burst trigger. A series of images were taken using the clear filter with 60 s exposures. Due to the poor weather condition, the optical afterglow was not detected in the stacked image after the standard correction procedure of bias and flat. Finally, an upper limit was obtained, calibrated with nearby stars in the USNO-B1.0 catalog, as mentioned in Table B4 of the appendix.

3.1.4 OSN

Eight hours after the burst trigger, we used the 1.5 m telescope at *Observatorio de Sierra Nevada* (OSN, Granada, Spain) to monitor the optical afterglow evolution of GRB 210619B (Hu et al. 2021). Four epochs observations were executed on 20-25 June 2021. In the first epoch, images in BVRI-filters with 90 s exposure each were obtained. The afterglow is clearly seen in the single-frame except for the B-band even after stacked. Therefore, the second and third epochs were obtained using 300 s exposures in RI-filters, but the afterglow was barely seen in single images. Even though the I-band images with 300 s exposures taken in order to get deep monitoring of it, it was indeed weakly seen in the stacked image. We analysed these imaging data with IRAF software using aperture photometry performed with standard procedures after bias and flat-field corrections. The magnitudes were calibrated using the reference stars in the same field of view from the Pan-STARRS catalog (Flewelling et al. 2020) with equations from Lupton et al. (2004) for the transformation between them. Results are shown in Table B4 of the appendix and Figure 15.

3.1.5 CAHA

We also triggered the 2.2 m telescope at Calar Alto Observatory located at Almeria, Spain. Using the onboard instrument Calar Alto Faint Object Spectrograph (CAFOS), images in Sloan-r filter (with 180 s exposure each) were obtained on 27 June 2021 starting at 02:59 UT, which is already about 8 days after the burst trigger. The optical afterglow is still detected in the stacked image. The reduction process followed standard procedures using the IRAF routine after bias and flat correction. Then the photometric results were calibrated with nearby stars from Pan-STARRS catalog (Flewelling et al. 2020). A full observation log is shown in Table B4 of the appendix.

3.1.6 GTC/OSIRIS: spectroscopic

We performed optical spectroscopy observations of GRB 210619B afterglow with the Optical System for Imaging and low-Resolution Integrated Spectroscopy (OSIRIS), mounted on the 10.4 m GTC, under the program GTCMULTIPLE2F-21A (PI: A. J. Castro-Tirado) on 25 June 2021. The observation consisted of 3x1200 s frames using the grism R2000B, which covers a spectral range from 3950 Å to 5700 Å as tabulated in Table B4 of the appendix.

We reduced the GTC/OSIRIS data using *PypeIt* v1.8.1[12] (Prochaska et al. 2022). This is an open-source Python-based spectroscopic data reduction pipeline (see Prochaska et al. 2020). Basic

---

[8] https://fermi.gsfc.nasa.gov/cgi-bin/ssc/LAT/LATDataQuery.cgi
[9] https://fermi.gsfc.nasa.gov/ssc/data/analysis/scitools/gtburst.html
[10] https://www.swift.ac.uk/xrt_curves/
[11] https://www.swift.ac.uk/xrt_spectra/

[12] https://github.com/pypeit/PypeIt/releases/tag/1.8.1

image processing (overscan, bias, flat-fielding, cosmic removal, etc.) followed standard techniques. Wavelength solutions (in vacuum, heliocentric frame) for individual images were computed from HgAr, Xe, and Na arc lamps. Flux calibration was derived from the G24-9 standard star. Given that the afterglow trace is not detected in the individual frames, we combined only the 2D frames with different spectral binnings (from 1 to 6 pixels) in order to find the best compromise between SNR and spectral resolution for the final 1D spectrum. However, we only detect (at best) a featureless, very low significance continuum at the position of the GRB afterglow. For the analysis reported hereafter, we have used the redshift value ($z = 1.937$) for GRB 210619B reported by De Ugarte Postigo et al. (2021) using an earlier GTC spectrum, obtained only 2.5 hr after the GRB detection.

3.1.7 GTC/OSIRIS: optical imaging

In order to get the deep image of the burst field, a late time follow-up observation was executed with the 10.4 m GTC under the same program on 9 July, i.e., 20 days after the trigger. During this epoch, the seeing was 1.6" which is not as good as expected, therefore, we carried out a second epoch deep imaging on 30 July, i.e. 41 days after the trigger. During this epoch, the seeing was 0.9", better than the first epoch observations. A series of images were taken using Sloan-griz filters with exposures of 90 s, 60 s, and 50 s, respectively. These images were analysed using the aperture photometry method after bias and flat correction with IRAF routines and calibrated with reference stars in the nearby field from the Pan-STARRS catalog. In our first epoch observations, the optical counterpart of GRB 210619B located in the UVOT/*Swift* error region was detected in the r band with a magnitude of 24.75 mag. However, in our second epoch of observations, we did not detect the optical counterpart of GRB 210619B, and we obtained an upper limit of r ∼ 25.7 mag.

In addition to our late-time photometric observations of the optical afterglow of GRB 210619B (see Table B4 of the appendix), for completeness, we also utilized those reported in Gamma-ray Coordination Network (see Table B5 of the appendix) in our analysis.

3.1.8 Host galaxy Search

On 10 July 2021, late-time observations of the burst took place with the 10.4 m GTC telescope. Then at 20 days post-trigger, a point-like source i.e., the afterglow was still clearly detected in the stacked images of each gri and z-bands at the UVOT position (Kuin et al. 2021). Later on, second epoch observations were taken on July 30, showing that the source faded beyond detection and no underlying object was found within the error region (see Figure 14). An excess of counts/signal in the late time r-band stacked image can be seen aligned in the direction of a nearby star's spark. Furthermore, the source position in redder filters, i.e., iz-bands, was out of the spark direction, and still, no credible detection was found. Therefore, we conclude that the host galaxy has not been detected during our two epochs' observations and that the host's brightness is fainter than our estimated upper limits (see Table B4 of the appendix). For this burst, the i-band absolute magnitude of <-19.5 mag, points to a fainter and perhaps dwarf galaxy host as discussed in Perley et al. (2016); Lyman et al. (2017).

3.2 Results

The present section highlights the broadband late-time afterglow features of GRB 210619B using our observations (see § 3.1) along with

those reported in the public domain (see Table B5 of the appendix). The broadband afterglow behaviour of GRBs could be understood either indirectly through empirical fitting constraining the temporal and spectral indices (closure relationship) or directly through external shock fireball modelling. Here, we have explored the empirical fitting method to understand the nature of the late-time broadband afterglow emission of GRB 210619B and have compared it with the afterglow results reported by Oganesyan et al. (2021).

3.2.1 Temporal and spectral evolution of X-ray and optical afterglows

The multi-wavelength afterglow light curve of GRB 210619B is shown in Figure 15 (top panel). The X-ray afterglow light curve of GRB 210619B does not show any flaring activity and could be fitted using a broken power-law function with the following temporal parameters: temporal index before the break $\alpha_{x,1} = 0.95 \pm 0.01$, temporal index after the break $\alpha_{x,2} = 1.49 \pm 0.03$, and break time $t_{x,b} = 12241 \pm 1141$ s ($\chi^2/d.o.f = 1397/1519$). We modelled the late time time-averaged (from $T_0 + 6394$ to $T_0 + 34829$ s) X-ray PC mode spectrum (early WT mode observations may not provide accurate column density due to the fluctuations) to constrain the intrinsic hydrogen column density and other X-ray spectral parameters of GRB 210619B. We obtained the following spectral parameters using time-integrated XRT observations: X-ray photon indices $\Gamma_{X-ray} = 1.90^{+0.06}_{-0.06}$, and intrinsic hydrogen column density $N_{H,z} = 9.25^{+3.01}_{-2.86} \times 10^{21}$ cm^{-2}. The bottom panel of Figure 15 shows the temporal evolution of X-ray photon indices during the entire X-ray afterglow emission phase. We noticed that the X-ray photon indices do not change during the entire XRT observations epochs (mean value of $\Gamma_{X-ray} = 1.81$). The observed temporal break in the X-ray afterglow light curve could be explained either due to the crossing of break frequencies or due to a possible jet break. However, as the spectral indices do not change, it supports the later scenario (jet break). Based on the above and in the light of applicable closure relationships for the ISM forward shock model, the X-ray afterglow of GRB 210619B seems to be consisted with normal decay phase followed by a jet break phase.

The late-time optical afterglow light curve of GRB 210619B using data from the present analysis and those published ones could be well described either by a single power-law (only the R band light curve due to unavailability of early, i.e. before the jet break, data in the same filter) or broken power-law functions. We have used the r-band light curve (longest and densest temporal coverage) to understand the temporal features of the optical emission of GRB 210619B. The foreground extinction corrected r-band light curve could be fitted using a broken power-law function with the following temporal parameters: temporal index before the break $\alpha_{r,1} = 0.61 \pm 0.04$, temporal index after the break $\alpha_{r,2} = 1.23 \pm 0.05$, and break time $t_{r,b} = 16076 \pm 3332$ s. We noticed that the break time in the optical light curve is consistent with the break time in the X-ray afterglow light curve.

3.2.2 Joint X-ray and optical SED evolution

We created joint spectral energy distributions (SEDs) to constrain the intrinsic host extinction and the X-ray and optical spectral indices (both before and after the jet break phase), as described below. Then, we utilized the closure relationships using temporal and spectral indices (both for optical and X-ray) in the ISM as well as WIND mediums (without energy injection from the central engine) to constrain the location of the cooling-break frequency (ν_c) and other afterglow properties.
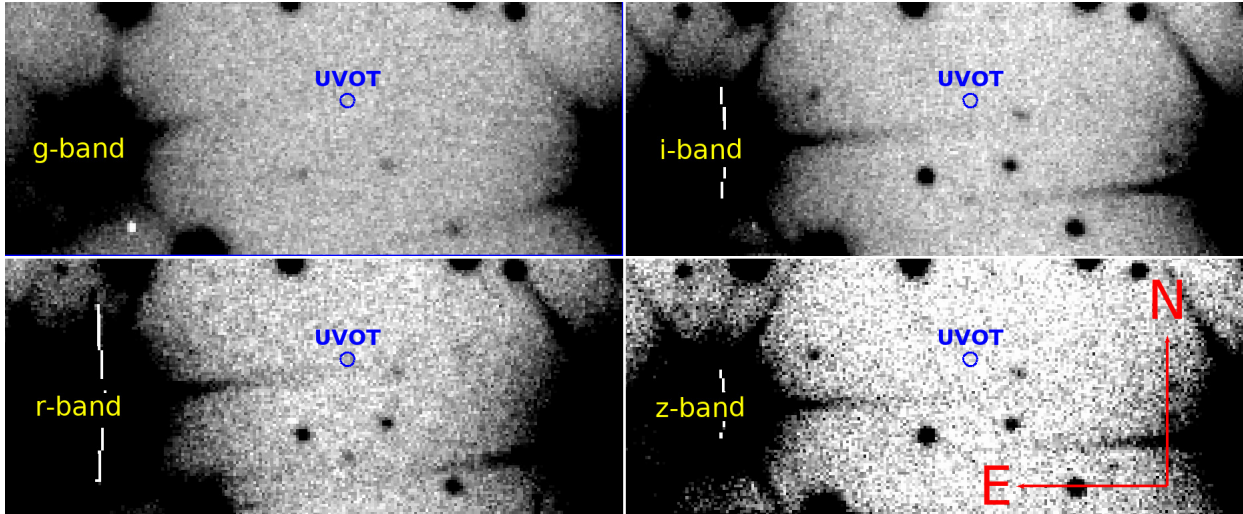
Figure 14. Late deep observation obtained with Sloan griz-filters by the 10.4 m GTC telescope on 29 July 2021 (i.e., ∼ 40 days after trigger) at the GRB 210619B field. The UVOT position is marked with the blue circle. There is no possibility of an existing underlying host galaxy detected within the UVOT error region. East is leftwards, and North is upwards.
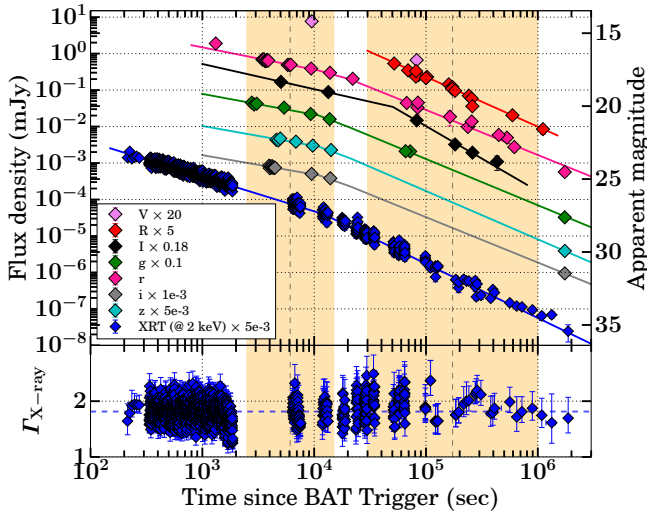

Figure 15. Multi-wavelength afterglow of GRB 210619B. Top panel: The various colored solid lines shows the empirical power-law or broken power-law model fitting to the observed data points. The optical data sets are corrected for the foreground extinction. Bottom panel: The temporal evolution of X-ray photon indices. The horizontal blue dashed line shows the mean value of the photon indices. The vertical orange shaded regions indicate the epochs of spectral energy distributions. The vertical black dashed lines show the corresponding centered epochs of both the SEDs.

We constructed two optical- X-ray SEDs centered at 6100 s and 173 ks. The first SED at 6100 s was constructed with the methodology of Schady et al. (2010), using data within a time range of 2500−15 ks. To construct the pha files for the different optical filters at 6100 s, we first constructed a single filter light curve by normalising the individual filter light curves together. Then using this single filter light curve, we determined the temporal slope within the 2500−15 ks interval. We then fitted a power-law to the individual filter light curves within this same time interval, fixing the slope to the value determined from the single filter light curve. We used the derived normalisations

to compute the count rate and count rate error at 6100 s, which was then applied to the relevant spectral file. For the XRT data, we have taken the PC mode spectral files built using the time-sliced spectra option on the Leicester *Swift* XRT webpage [13] (Evans et al. 2009). The spectral files were normalized to correspond to the 0.3 − 10 keV flux of the afterglow at the mid point of the selected time range. The flux, used to normalize a given spectrum, was determined by fitting a power-law to the temporal data within the SED selected time range. The best-fit decay index was used to compute the flux at the mid-point of the SED, in the same way as was done for the optical data. The optical pha files for the second SED centered at 173 ks, were constructed directly from the GTC magnitudes taken at that time, assuming the data are quasi-simultaneous. The X-ray data for the second SED was constructed using the same methodology as the 6100 s SED, except that the data were extracted from 30000 − 10^6 s and normalised to 173 ks.

Both SEDs were fitted using XSPEC (version 12.12.0), following the procedure outlined in Schady et al. (2010, 2007). We tested two different models for the continuum: a power-law and a broken power-law, with the change in spectral slope fixed to be $\Delta\beta = 0.5$ for the broken-power law component, which corresponds to the expected change in spectral slope caused by the synchrotron cooling frequency (Sari et al. 1998). In each of these models, we also included two dust and gas components to account for the Galaxy and host galaxy dust extinction and photoelectric absorption (*phabs*, *zphabs*, *zdust*; we used *zdust* for both the Galaxy and host galaxy dust components, but with the redshift set to zero for the Galaxy dust component). The Galactic components were frozen to the reddening and column density values from Schlegel et al. (1998) and Kalberla et al. (2005), respectively. For the host galaxy dust extinction, we tested the dependence of dust extinction on wavelength for three different scenarios: the Small and Large Magellanic clouds (SMC and LMC, respectively) and on the Milky Way (MW). In addition, we also accounted for the absorption due to the Lyman series in the 912 − 1215 Å restframe wavelength range, with the XSPEC *zigm* component. We set this component to used the prescription of Madau (1995) to estimate

---

[13] https://www.swift.ac.uk/xrt_spectra

Figure 17. Delayed LAT emission: Distribution of high energy GeV photons observed by *Fermi* LAT from GRB 210619B. The colored squares and diamond shows the probability of individual photons to be associated with GRB 210619B. The blue dashed line represents the maximum possible high energy GeV energy using the synchrotron process.

power-law for each of the three extinction curves. In this case, the $\chi^2/d.o.f$ for the LMC and SMC fits are very similar and slightly preferred over the MW. Given the preference for the SMC in the first SED, we assume this as the best extinction curve for the 173 ks SED. The F-test on SMC power-law ($\chi^2/d.o.f = 147/90$) and SMC broken power-law ($\chi^2/d.o.f = 92/89$) gives a p-value of $<< 10^{-5}$, suggesting the break is statistically required. Overall, for both the SEDs, we take the best fit model as the broken power-law, with SMC type extinction.

3.2.3 GeV afterglow and Comparison with LAT catalog

Figure 17 shows the distribution of the high energy photons and their association with GRB 210619B, detected by *Fermi* LAT. *Fermi* LAT observed the highest-energy photon at ~ 410 s post *Fermi* trigger with an energy of 8.38 GeV (Axelsson et al. 2021). During the time window of our LAT analysis ($T_0 + 285$ s to $T_0 + 10$ ks), we found the following spectral parameters: energy flux = $(4.35 \pm 2.15) \times 10^{-10}$ erg cm^{-2} s^{-1} (in 100 MeV - 10 GeV energy range), photon flux = $(2.38 \pm 1.52) \times 10^{-7}$ ph. cm^{-2} s^{-1} (in 100 MeV - 10 GeV energy range), the LAT photon index (Γ_{LAT}) = -1.42 ± 0.28 with the test-statistic (TS) of detection = 30. During this window, we noticed that there were only a few GeV photons (> 100 MeV) with probability larger than 90 % to be associated with GRB 210619B. To constrain the possible emission process of GeV photons, we used equation 9 from Piran & Nakar (2010) to estimate the maximum energy emitted by the synchrotron process during the decelerating phase in the case of ISM-like ambient medium. We noticed that all the GeV photons observed from GRB 210619B with associated probability greater than 50 % could be described using synchrotron emission.

In the top panel of Figure B2 of the appendix, we have plotted the distribution of the maximum energy of the highest-energy LAT photons with respect to the arrival time for GRB 210619B. We have also shown the other LAT detected GRBs data points obtained from the second *Fermi* LAT GRB Catalog (2FLGC). In the
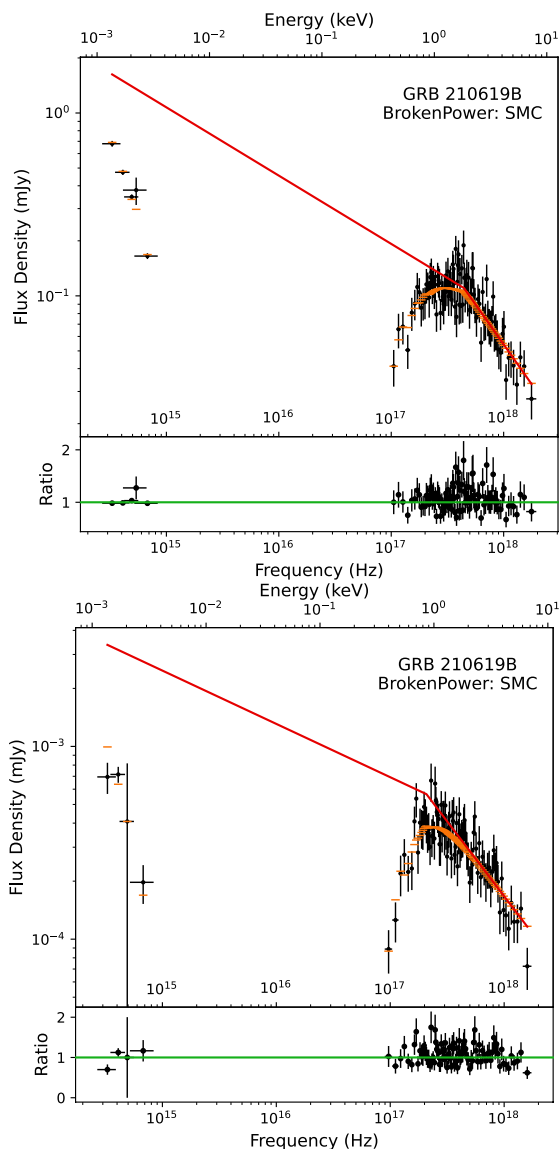

Figure 16. Joint X-ray and optical SED of GRB 210619B. Top panel: SED 1 centered at 6100 s (T_0 +2500 to T_0 +15 ks) (plus optical data in Vrigz filters; data from Figure 15) and Bottom panel: SED 2 centered at 173 ks using XRT data from (T_0 +30 ks to T_0 + 10^6 s) plus optical data in griz filters from GTC. Both SEDs were the best fit using the broken power-law model with the SMC as the best fit host extinction law. The host galaxy absorbed and extinguished spectral model points are given in orange and the best-fit absorption and extinction corrected spectral model is given by the solid red line. The ratio of the data divided by the folded model is given in the sub-panel of each panel.

the effective optical depth from the Lyman series as a function of wavelength and redshift, and we set this component to also include attenuation due to photoelectric absorption.

The results of the SED fits are shown in Figure 16 and tabulated in Table 5. For the 6100 s, for both the power-law and broken power-law, the SMC type extinction gives the best fit, for the power-law model the fit gives $\chi^2/d.o.f = 170/95$, while for the broken power-law model the fit gives $\chi^2/d.o.f = 87/94$. An F-test gives a p-value of $<< 10^{-5}$, suggesting the break is statistically required. For the 173 ks SED, for the power-law model the fits with the 3 different extinction laws give similar $\chi^2/d.o.f$, however, the MW extinction law is preferred. The broken power-law model gives a smaller $\chi^2/d.o.f$ compared to the
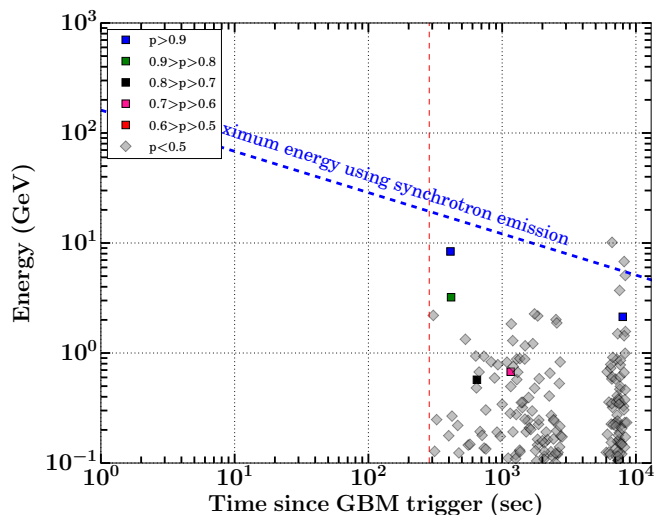
Table 5. Results from simultaneous UV/optical and X-ray spectral fits for the SMC, LMC, and MW dust-extinction law models, for both a power-law (POW) and a broken power-law (BKP) continuum. For the broken power-law model, the second spectral index is fixed as $\beta_2 = \beta + 0.5$. The fourth and fifth columns give the host galaxy equivalent column density and E(B-V), the sixth column gives the break energy for the broken power-law spectral models, the χ^2 and degree of freedom (dof) of the fit are given in the seventh column, and the eighth gives the null hypothesis probability.

SED	Model	β	N_H 10^{21} cm^{-2}	E(B-V) (mag)	E_{bk} (keV)	χ^2 (dof)	Null Hypothesis Probability
6100 s	MW/POW	$0.47^{+0.01}_{-0.01}$	$0.60^{+1.70}_{-0.60}$	$0.24^{+0.01}_{-0.01}$	–	378 (95)	<1e-05
6100 s	LMC/POW	$0.45^{+0.01}_{-0.01}$	$0.27^{+1.65}_{-0.27}$	$0.19^{+0.01}_{-0.01}$	–	184 (95)	<1e-05
6100 s	SMC/POW	$0.41^{+0.00}_{-0.01}$	< 3.95	$0.15^{+0.01}_{-0.01}$	–	170 (95)	<1e-05
6100 s	MW/BKP	$0.42^{+0.02}_{-0.02}$	$4.80^{+2.13}_{-1.98}$	$0.21^{+0.01}_{-0.01}$	$2.02^{+0.20}_{-0.18}$	319 (94)	<1e-05
6100 s	LMC/BKP	$0.42^{+0.01}_{-0.01}$	$5.42^{+2.15}_{-1.98}$	$0.18^{+0.01}_{-0.01}$	$1.93^{+0.19}_{-0.16}$	116 (94)	0.06
6100 s	SMC/BKP	$0.37^{+0.01}_{-0.01}$	$4.24^{+2.12}_{-1.94}$	$0.14^{+0.01}_{-0.01}$	$1.84^{+0.17}_{-0.17}$	87 (94)	0.695
173 ks	MW/POW	$0.72^{+0.05}_{-0.05}$	$7.90^{+2.45}_{-2.23}$	$0.73^{+0.08}_{-0.07}$	–	146 (90)	1.86e-04
173 ks	LMC/POW	$0.74^{+0.06}_{-0.05}$	$8.63^{+2.62}_{-2.41}$	$0.72^{+0.08}_{-0.08}$	–	146 (90)	1.84e-04
173 ks	SMC/POW	$0.76^{+0.05}_{-0.05}$	$9.52^{+2.61}_{-2.41}$	$0.79^{+0.08}_{-0.08}$	–	147 (90)	1.37e-04
173 ks	MW/BKP	$0.34^{+0.04}_{-0.04}$	$8.79^{+3.10}_{-3.77}$	$0.32^{+0.05}_{-0.05}$	$0.82^{+0.27}_{-0.16}$	100 (89)	0.205
173 ks	LMC/BKP	$0.31^{+0.04}_{-0.03}$	$7.50^{+2.78}_{-3.37}$	$0.25^{+0.04}_{-0.04}$	$0.84^{+0.25}_{-0.14}$	91 (89)	0.413
173 ks	SMC/BKP	$0.28^{+0.04}_{-0.03}$	$5.95^{+2.36}_{-3.08}$	$0.21^{+0.04}_{-0.04}$	$0.86^{+0.23}_{-0.13}$	92 (89)	0.403

case of GRB 210619B, the highest-energy GeV photon detected by *Fermi* LAT arrived after the *Fermi* GBM T_{90} duration, in agreement with a large fraction of *Fermi* LAT detected bursts. Furthermore, we also measured the restframe isotropic γ-ray energy in the 100 MeV - 10 GeV ($E_{\text{LAT,iso}}$) using *Fermi* LAT observations for GRB 210619B. We have shown the distribution of $E_{\text{LAT,iso}}$ with respect to redshift (z) for GRB 210619B and have compared 34 other LAT detected GRBs with their measured redshift from the 2FLGC (see bottom panel of Figure B2 in the appendix). We notice that GRB 210619B is a moderately energetic event amongst the *Fermi* LAT detected GRB at $z \sim 2$, with the highest-energy photon at 16.76 GeV in the source restframe.

3.3 Discussion

Based on the above mentioned results using the multi-wavelength analysis of the afterglow properties of GRB 210619B, our major findings are discussed below in the following sub-sections.

3.3.1 Closure relations and cooling break frequency

We implemented closure relations before and after the jet break phase of GRB 210619B, following the predictions of the fireball model without energy injection from the central engine (Racusin et al. 2009; Gao et al. 2013; Wang et al. 2018). These "closure relations" depend on properties like jet geometry, electron energy index (p), spectral regimes (slow/fast) and the surrounding environment (Sari et al. 1998; Piran 2004). Our joint optical and SED fitting (see § 3.2.2) before the jet break phase clearly indicates a break (1.84 ± 0.17 keV) in the SED within the X-ray band (see the top panel of Figure 16). Assuming the break due to cooling break frequency and the slow cooling case for an ISM like ambient medium for $p > 2$ (**a softer power-law (non-thermal) distribution of the shock-accelerated electrons**), we have also explored various other possible spectral regimes; however, we noticed that the first SED could be well explained using $\nu_m < \nu_c < \nu_x$ (where ν_m, ν_c, and ν_x are the synchrotron peak, cooling-break, and X-ray frequencies, respectively) spectral regime for the ISM slow cooling case. For this spectral regime, we calculated the X-ray, i.e. $\alpha_x = 3(\beta_x-1)/2$, and optical ($\alpha_o = 3\beta_o/2$) temporal indices using their observed values of spectral indices and found $\alpha_x = 0.81 \pm 0.02$ and $\alpha_o = 0.56 \pm 0.02$. These predicted values of X-ray and optical temporal indices

are smaller than the observed ones. Using the calculated value of the X-ray spectral index, we estimated the p value of $p = 1.74 \pm 0.02$ (a smaller value with respect to normally observed cases, i.e. $p > 2$). Therefore we also examined the "closure relation" for the same spectral regime but for harder electron energy index case (with $1 < p < 2$; Resmi & Bhattacharya 2008; Racusin et al. 2009). In this case, we calculated $\alpha_x = 0.95 \pm 0.01$ and $\alpha_o = 0.70 \pm 0.01$ using the observed values of X-ray and optical spectral indices, respectively. We noticed that these values are well in agreement with the observed values ($\alpha_x = 0.95 \pm 0.01$ and $\alpha_o = 0.61 \pm 0.04$). However Oganesyan et al. (2021) considered similar values (without host galaxy reddening correction) of optical/X-ray spectral indices ($\beta_x=\beta_o=0.9$) and claimed that at least before the jet break phase the observed ν_c is above the X-ray band, which is inconsistent with our findings and are ruled out by our SED fitting (see § 3.2.2). Additionally we also implemented the "closure relations" post jet break phase and noticed that ν_c follows the typical evolution predicted post jet break phase (i.e. t^0) which remains close to the XRT spectral window ($\beta_x=\beta_o+0.5$) throughout the afterglow emission phase. The derived value of β_o using near-simultaneous griz observations with the 10.4 m GTC at very late epochs, i.e., ~ 20 days post burst, are also consistent with post jet break forward shock model predictions.

4 SUMMARY AND CONCLUSIONS

In this work, we present a detailed analysis of the prompt emission plus thermal and spectral characteristics of a long, luminous, and peculiar multi-structured burst GRB 210619B (which was also observed by the Atmosphere-Space Interactions Monitor installed on the International Space Station). The prompt light curve shows a very bright and brief pulse (~ 4 s) followed by softer and rather long emission episodes up to ~ 65 s. A detailed time-resolved spectral analysis indicates hard low-energy photon indices, exceeding the synchrotron LOD in most of the Bayesian bins with high significance during brighter pulses, and it becomes softer (within the error bar) during the longer/softer emission phase. Harder α_{pt} values observed during brighter emission pulses could be attributed to thermal emission arising from photospheric regions. On the other hand, the softer values of the low-energy photon indices during the longer emission phase are consistent with the non-thermal thin shell synchrotron emission model. This suggests that the radiation process responsible for GRB 210619B shows a transition between photospheric thermal

emission (hard α_{pt}) and non-thermal synchrotron emission (soft α_{pt}). In addition, we noticed a peculiar spectral evolution of E_p and α_{pt}, where both of these spectral parameters exhibit the 'flux tracking' pattern. We found strong/moderate positive correlations among various parameters: log (Flux)-log (E_p), log (Flux)-α_{pt}, and log (E_p)-α_{pt}, supporting the observed tracking pattern of the E_p and α_{pt}. The flux tracking behaviour of E_p could be understood in terms of cooling and expansion of the fireball. In such scenario, during the cooling of relativistic electrons, the magnetic field and electron energy will decrease, resulting in a lower intensity and E_p values; however, during the expansion of the fireball, the magnetic field and electron energy will increase, giving rise to higher intensity and E_p values (Gupta et al. 2021). On the other hand, the flux tracking behaviour of α_{pt} could be understood in terms of photospheric heating in a flow with a varying entropy (Ryde et al. 2019). We also observed a negative spectral lag for this burst, thus being an outlier of typical known lag-luminosity anti-correlation of long bursts. The observed negative spectral lag could be explained in terms of a superposition of effects, thus being consistent with the observed intensity tracking behaviour (spectral evolution) of the peak energy. We produced the joint SED using XRT and optical photometric data and constrained the location of cooling frequency and host extinction of GRB 210619B. We observed that the SED could be described within the framework of an external forward shock model with $\nu_m < \nu_c < \nu_x$ spectral regime supporting the rarely observed hard electron energy index (with $p < 2$) in an ISM-like ambient medium. **The hard electron energy index indicates a flat spectrum (a harder power-law distribution of the shock-accelerated electrons) at higher frequencies and can be explained in terms of two possible scenarios. The first case is a single power-law distribution of electrons ($1 < p < 2$) having an exponential cutoff corresponding to maximum electron Lorentz factor (Bhattacharya 2001); and the second scenario being a double power-law distribution of electrons ($1 < p1 < 2$ and $p2 > 2$) having an "injection break" (Panaitescu & Kumar 2001; Bhattacharya & Resmi 2004; Resmi & Bhattacharya 2008). More such GRBs using ASIM and other space-based high energy instruments would be useful to decipher such evolution of p giving rise to additional piece of information to understand particle acceleration and shock physics in more detail.**

DATA AVAILABILITY

The data presented in this work can be made available based on the individual request to the corresponding authors.

REFERENCES

Agostinelli S., et al., 2003, Nucl. Instr. and Meth. A, 506, 250

Amati L., 2006, MNRAS, 372, 233

Arnaud K. A., 1996, in Jacoby G. H., Barnes J., eds, Astronomical Society of the Pacific Conference Series Vol. 101, Astronomical Data Analysis Software and Systems V. p. 17

Atwood W. B., et al., 2009, ApJ, 697, 1071

Axelsson M., Pillera R., Longo F., Fermi-LAT Collaboration 2021, GRB Coordinates Network, 30270, 1

Band D., et al., 1993, ApJ, 413, 281

Barthelmy S. D., et al., 2005, Space Sci. Rev., 120, 143

Beardmore A. P., Evans P. A., Goad M. R., Osborne J. P., Swift-XRT Team. 2021, GRB Coordinates Network, 30267, 1

Belkin S., Pozanenko A., Inasaridze R. Y., Ayvazian V. R., Kapanadze G. V., Pankov N., IKI GRB FuN 2021a, GRB Coordinates Network, 30299, 1

Belkin S., Pozanenko A., Burhonov O., Kim V., Krugov M., Pankov N., Ehgamberdiev S., IKI-GRB-FuN 2021b, GRB Coordinates Network, 30791, 1

Beloborodov A. M., Mészáros P., 2017, Space Sci. Rev., 207, 87

Bernardini M. G., et al., 2015, MNRAS, 446, 1129

Bhat P. N., et al., 2016, VizieR Online Data Catalog, p. J/ApJS/223/28

Bhattacharya D., 2001, Bulletin of the Astronomical Society of India, 29, 107

Bhattacharya D., Resmi L., 2004, in Feroci M., Frontera F., Masetti N., Piro L., eds, Astronomical Society of the Pacific Conference Series Vol. 312, Gamma-Ray Bursts in the Afterglow Era. p. 411 (arXiv:astro-ph/0301379)

Burgess J. M., 2014, MNRAS, 445, 2589

Burgess J. M., Bégué D., Greiner J., Giannios D., Bacelj A., Berlato F., 2020, Nature Astronomy, 4, 174

Burrows D. N., et al., 2005, Space Sci. Rev., 120, 165

Campana S., et al., 2006, Nature, 442, 1008

Castro-Tirado A. J., et al., 2012, in Astronomical Society of India Conference Series. pp 313–320

Castro-Tirado A. J., et al., 2021, Nature, 600, 621

Chakrabarti A., Chaudhury K., Sarkar S. K., Bhadra A., 2018, Journal of High Energy Astrophysics, 18, 15

Chand V., Pal P. S., Banerjee A., Sharma V., Tam P. H. T., He X., 2020, ApJ, 903, 9

Chanrion O., et al., 2019, Space Sci. Rev., 215, 28

Crider A., et al., 1997, ApJ, 479, L39

D'Avanzo P., Bernardini M. G., Lien A. Y., Melandri A., Page K. L., Palmer D. M., Sbarrato T., Neil Gehrels Swift Observatory Team 2021a, GRB Coordinates Network, 30261, 1

D'Avanzo P., Melandri A., Covino S., Fugazza D., REM Team 2021b, GRB Coordinates Network, 30288, 1

De Ugarte Postigo A., et al., 2021, GRB Coordinates Network, 30272, 1

Dermer C. D., 2004, ApJ, 614, 284

Evans P. A., et al., 2007, A&A, 469, 379

Evans P. A., et al., 2009, MNRAS, 397, 1177

Flewelling H. A., et al., 2020, ApJS, 251, 7

Foreman-Mackey D., Hogg D. W., Lang D., Goodman J., 2013, PASP, 125, 306

Gao H., Lei W.-H., Zou Y.-C., Wu X.-F., Zhang B., 2013, New Astron. Rev., 57, 141

Gehrels N., et al., 2004, ApJ, 611, 1005

Goldstein A., et al., 2017, ApJ, 848, L14

Golkhou V. Z., Butler N. R., Littlejohns O. M., 2015, ApJ, 811, 93

Gruber D., et al., 2014, ApJS, 211, 12

Guiriec S., et al., 2011, ApJ, 727, L33

Gupta R., et al., 2021, MNRAS, 505, 4086

Gupta R., et al., 2022, MNRAS, 511, 1694

Hjorth J., et al., 2003, Nature, 423, 847

Hu Y. D., Sota A., Sun T. R., Castro-Tirado A. J., Caballero-Garcia M. D., Castro Tirado M. A., Fernandez-Garcia E., 2021, GRB Coordinates Network, 30293, 1

Iyyani S., 2018, Journal of Astrophysics and Astronomy, 39, 75

Kalberla P. M. W., Burton W. B., Hartmann D., Arnal E. M., Bajaja E., Morras R., Pöppel W. G. L., 2005, A&A, 440, 775

Kann D. A., de Ugarte Postigo A., Blazek M., Thoene C., Agui Fernandez J. F., Ginger Vico Linares J. I., 2021a, GRB Coordinates Network, 30275, 1

Kann D. A., de Ugarte Postigo A., Jelinek M., Blazek M., Thoene C., Agui Fernandez J. F., Minguez P., 2021b, GRB Coordinates Network, 30338, 1

Kargatis V. E., Liang E. P., Hurley K. C., Barat C., Eveno E., Niel M., 1994, ApJ, 422, 260

Kawakubo Y., et al., 2021, GRB Coordinates Network, 30284, 1

Klebesadel R. W., Strong I. B., Olson R. A., 1973, ApJ, 182, L85

Kong A. K. H., 2021, GRB Coordinates Network, 30265, 1

Kuin N. P. M., D'Avanzo P., Swift/UVOT Team 2021, GRB Coordinates Network, 30278, 1

Kumar P., Zhang B., 2015, Phys. Rep., 561, 1

Kumar H., Stanzin U., Bhalerao V., Anupama G. C., Barway S., GIT Team 2021, GRB Coordinates Network, 30286, 1

Levin V., Molkov S., Mereminskiy I., Lutovinov A., Semena A., Filippova E., SRG/ART-XC Team 2021, GRB Coordinates Network, 30283, 1

Li L., 2019, ApJS, 242, 16

Li L., et al., 2019, ApJ, 884, 109

Li L., Ryde F., Pe'er A., Yu H.-F., Acuner Z., 2021, ApJS, 254, 35

Liang E.-W., Yi S.-X., Zhang J., Lü H.-J., Zhang B.-B., Zhang B., 2010, ApJ, 725, 2209

Lindanger A., et al., 2021, JOURNAL OF GEOPHYSICAL RESEARCH-ATMOSPHERES, 126

Lupton R., Blanton M. R., Fekete G., Hogg D. W., O'Mullane W., Szalay A., Wherry N., 2004, PASP, 116, 133

Lyman J. D., et al., 2017, MNRAS, 467, 1795

Lyutikov M., Blackman E. G., 2001, MNRAS, 321, 177

Madau P., 1995, ApJ, 441, 18

Marisaldi M., Mezentsev A., Østgaard N., Reglero V., Neubert T., ASIM Team 2021, GRB Coordinates Network, 30315, 1

Medvedev M. V., 2000, ApJ, 540, 704

Meegan C., et al., 2009, ApJ, 702, 791

Meszaros P., Rees M. J., 1993, ApJ, 405, 278

Mészáros P., Rees M. J., 1997, ApJ, 482, L29

Minaev P. Y., Pozanenko A. S., 2020, MNRAS, 492, 1919

Minaev P. Y., Pozanenko A. S., Molkov S. V., Grebenev S. A., 2014, Astronomy Letters, 40, 235

Minaev P., Pozanenko A., Chelovekov I., Grebenev S., IKI GRB FuN 2021, GRB Coordinates Network, 30304, 1

Moskvitin A. S., Maslennikova O. A., GRB follow-up Team. 2021a, GRB Coordinates Network, 30291, 1

Moskvitin A. S., Maslennikova O. A., GRB follow-up Team. 2021b, GRB Coordinates Network, 30303, 1

Moskvitin A. S., Maslennikova O. A., GRB follow-up Team. 2021c, GRB Coordinates Network, 30309, 1

Nava L., et al., 2012, MNRAS, 421, 1256

Neubert T., et al., 2019, arXiv e-prints, p. arXiv:1906.12178

Norris J. P., Share G. H., Messina D. C., Dennis B. R., Desai U. D., Cline T. L., Matz S. M., Chupp E. L., 1986, ApJ, 301, 213

Norris J. P., Marani G. F., Bonnell J. T., 2000, ApJ, 534, 248

Oganesyan G., et al., 2021, arXiv e-prints, p. arXiv:2109.00010

Østgaard N., et al., 2019, Space Sci. Rev., 215, 23

Page K. L., et al., 2021, GRB Coordinates Network, 30269, 1

Panaitescu A., Kumar P., 2001, ApJ, 554, 667

Pe'er A., 2015, Advances in Astronomy, 2015, 907321

Perley D. A., 2021, GRB Coordinates Network, 30271, 1

Perley D. A., et al., 2016, ApJ, 817, 8

Petropoulou M., Beniamini P., Vasilopoulos G., Giannios D., Barniol Duran R., 2020, MNRAS, 496, 2910

Piran T., 2004, Reviews of Modern Physics, 76, 1143

Piran T., Nakar E., 2010, ApJ, 718, L63

Poolakkil S., Meegan C., Fermi GBM Team 2021, GRB Coordinates Network, 30279, 1

Preece R. D., Briggs M. S., Mallozzi R. S., Pendleton G. N., Paciesas W. S., Band D. L., 1998, ApJ, 506, L23

Prochaska J., et al., 2020, The Journal of Open Source Software, 5, 2308

Prochaska J. X., et al., 2022, pypeit/PypeIt: Version 1.8.1, Zenodo, doi:10.5281/zenodo.3506872

Racusin J. L., et al., 2009, ApJ, 698, 43

Ravasio M. E., Ghirlanda G., Nava L., Ghisellini G., 2019, A&A, 625, A60

Resmi L., Bhattacharya D., 2008, MNRAS, 388, 144

Romanov F. D., 2021, GRB Coordinates Network, 30292, 1

Romanov F. D., Lane D. J., 2021, GRB Coordinates Network, 30305, 1

Ryde F., 2005, ApJ, 625, L95

Ryde F., Svensson R., 1999, ApJ, 512, 693

Ryde F., Yu H.-F., Dereli-Bégué H., Lundman C., Pe'er A., Li L., 2019, MNRAS, 484, 1912

Sari R., Piran T., Narayan R., 1998, ApJ, 497, L17

Scargle J. D., Norris J. P., Jackson B., Chiang J., 2013, arXiv e-prints, p. arXiv:1304.2818

Schady P., et al., 2007, MNRAS, 377, 273

Schady P., et al., 2010, MNRAS, 401, 2773

Schlegel D. J., Finkbeiner D. P., Davis M., 1998, ApJ, 500, 525

Sharma V., Iyyani S., Bhattacharya D., 2021, ApJ, 908, L2

Shrestha M., Gomboc A., Guidorzi C., Kobayashi S., Melandri A., Mundell C., Smith R., Steele I. A., 2021, GRB Coordinates Network, 30280, 1

Svinkin D., et al., 2021, GRB Coordinates Network, 30276, 1

Tak D., Guiriec S., Uhm Z. L., Yassine M., Omodei N., McEnery J., 2019, ApJ, 876, 76

Uhm Z. L., Zhang B., 2016, ApJ, 825, 97

Uhm Z. L., Zhang B., Racusin J., 2018, ApJ, 869, 100

Ukwatta T. N., et al., 2010, The Astrophysical Journal, 711, 1073–1086

Usov V. V., 1992, Nature, 357, 472

Vianello G., et al., 2015, arXiv e-prints, p. arXiv:1507.08343

Vianello G., Gill R., Granot J., Omodei N., Cohen-Tanugi J., Longo F., 2018, ApJ, 864, 163

Vinko J., et al., 2021, GRB Coordinates Network, 30320, 1

Von Kienlin A., et al., 2020, ApJ, 893, 46

Wang X.-G., Zhang B., Liang E.-W., Lu R.-J., Lin D.-B., Li J., Li L., 2018, ApJ, 859, 160

Woosley S. E., 1993, ApJ, 405, 273

Xin L. P., et al., 2021, GRB Coordinates Network, 30277, 1

Yonetoku D., Murakami T., Tsutsui R., Nakamura T., Morihara Y., Takahashi K., 2010, PASJ, 62, 1495

Yu H.-F., Dereli-Bégué H., Ryde F., 2019, ApJ, 886, 20

Zhang B., 2014, International Journal of Modern Physics D, 23, 1430002

Zhang B., 2020, Nature Astronomy, 4, 210

Zhang B. B., et al., 2018, Nature Astronomy, 2, 69

Zhao Y., et al., 2021, GRB Coordinates Network, 30264, 1

Zhu Z. P., de Ugarte Postigo A., Malesani D. B., Izzo L., Kann D. A., Xu D., Djupvik A. A., 2021, GRB Coordinates Network, 30294, 1

APPENDIX A: DETECTORS/TELESCOPES DESCRIPTION

A1 *Fermi* GBM and LAT instruments

The *Fermi* Gamma-ray Burst Monitor (GBM; Meegan et al. 2009) has twelve sodium iodide (NaI) and bismuth germanate (BGO) detectors, covering an energy range approximately from 8 keV to 1 MeV and 200 keV to 40 MeV, respectively. These detectors are arranged in such a way that GBM covers approximately all-sky, not hidden by the Earth, making it a crucial GRB detecting instrument with a large energy coverage. On the other hand, *Fermi* Large Area Telescope (LAT; Atwood et al. 2009) is a Gigaelectron-Volts (GeV) instrument working from 20 MeV to 300 GeV with a wide field of view (FoV).

A2 ASIM instrument

The Atmosphere-Space Interactions Monitor (ASIM; Neubert et al. 2019) is a mission of the European Space Agency (ESA) mounted on the starboard side of the Columbus module of the International Space Station (*ISS*) and operational since 2018. The main science objectives of the ASIM mission are Terrestrial Gamma-ray Flashes (TGF) and Transient Luminous Events (TLE), atmospheric phenomena associated with lightning activity. However, ASIM proved effective also in the detection of cosmic GRBs and similar phenomena (Castro-Tirado et al. 2021). The ASIM payload consists of two nadir-viewing instruments: the Modular X- and Gamma-ray Sensor (MXGS; Øst-gaard et al. 2019) and the Modular Multispectral Imaging Assembly (MMIA; Chanrion et al. 2019). MXGS consists of two detection planes: the Low Energy Detector (LED) based on Cadmium-Zinc Telluride (CZT) crystals, sensitive in the 50-400 keV range, and the High-Energy Detector (HED) made of 12 crystals of Bismuth Germanium Oxide (BGO) with photomultiplier readout. HED is sensitive to photons between 300 keV and >30 MeV. Data download is enabled by a trigger logic active on time scales spanning from 300 μs to 20 ms, tailored for the detection of sub-millisecond transients such as TGFs. When a trigger is issued, event data for a two-second time frame centered at trigger time are sent to telemetry for subsequent download.

A3 *Swift* BAT instrument

The Burst Alert Telescope (BAT; Barthelmy et al. 2005) on-board the Neil Gehrels Swift Observatory (*Swift*; Gehrels et al. 2004) mission is a highly sensitive coded aperture telescope (with a large FoV) designed to detect GRBs. It works in the energy range from 15-350 keV.

APPENDIX B: FIGURES AND TABLES
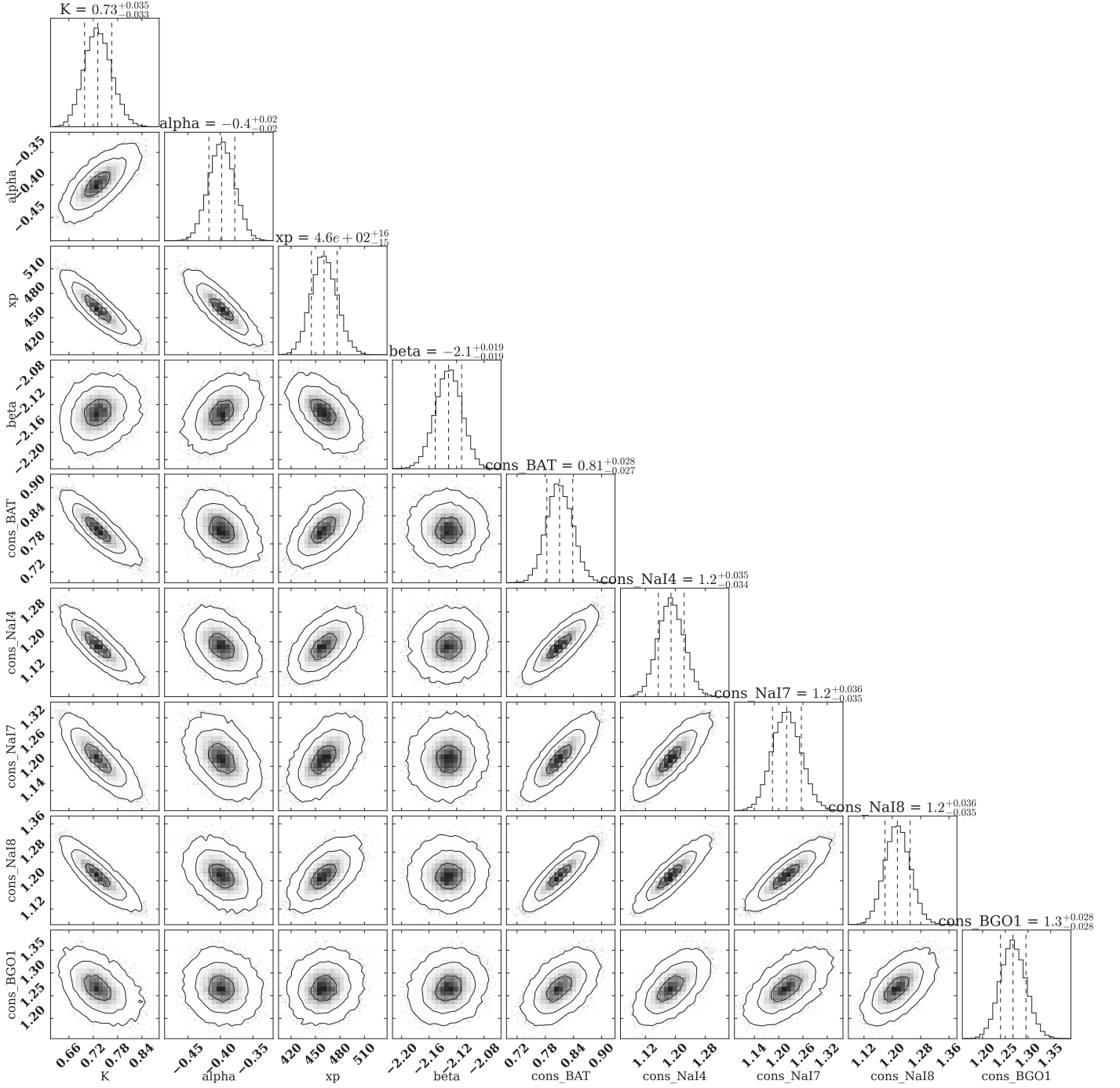
Figure B1. The corner plot of the best fit (Band) joint *Swift* BAT, *Fermi* GBM, and ASIM spectrum ($T_{0,ASIM}$+1.00 to $T_{0,ASIM}$+ 1.70 s) for 5000 number of simulations.
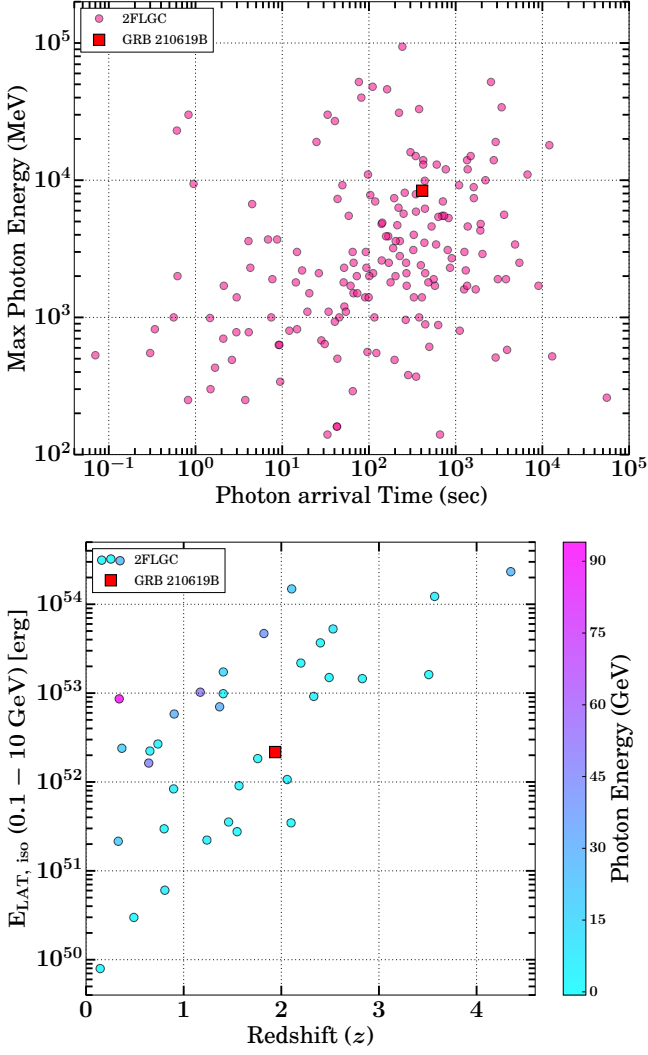
Figure B2. The comparison of GRB 210619B (shown with red squares) with second *Fermi* LAT GRB catalog (2FLGC). Top panel: GeV photons arrival time as a function of maximum energy. Bottom panel: Restframe isotropic energy in LAT energy range as a function of redshift.

Table B1: Results of the time-resolved prompt emission spectral analysis of GRB 210619B using Band and CPL functions and *Fermi* GBM data. The energy flux values (in erg cm^{-2} s^{-1}) are calculated in 8 keV-40 MeV energy range. The notation S denotes the significance of the spectrum of each time bin.

T$_{start}$ (s)	T$_{stop}$ (s)	S	α_{pt}	β_{pt}	E$_p$ (keV)	(Flux ×10^{-06})	DIC$_{Band}$	Γ_{CPL}	E$_c$ (keV)	(Flux ×10^{-06})	DIC$_{CPL}$	Δ DIC
0.068	0.213	39.61	$-0.17^{+0.09}_{-0.10}$	$-1.86^{+0.06}_{-0.06}$	$467.71^{+50.36}_{-49.46}$	77.32	100.11	$-0.45^{+0.05}_{-0.05}$	$530.00^{+49.80}_{-49.55}$	32.6	151.29	-51.18
0.213	0.302	41.06	$-0.24^{+0.09}_{-0.09}$	$-1.83^{+0.06}_{-0.06}$	$446.77^{+51.20}_{-50.90}$	107.36	-453.79	$-0.55^{+0.04}_{-0.04}$	$603.21^{+56.72}_{-56.25}$	46.82	-403.6	-50.19
0.302	0.397	55.82	$-0.36^{+0.06}_{-0.07}$	$-2.01^{+0.07}_{-0.07}$	$496.58^{+44.12}_{-43.73}$	114.85	-290.18	$-0.57^{+0.03}_{-0.03}$	$554.48^{+42.52}_{-42.29}$	60.7	-230.91	-59.27
0.397	0.502	73.81	$-0.35^{+0.06}_{-0.06}$	$-2.20^{+0.09}_{-0.09}$	$493.20^{+40.49}_{-39.94}$	115.28	-67.78	$-0.58^{+0.03}_{-0.03}$	$544.08^{+37.99}_{-38.24}$	78.1	-33.02	-34.76
0.502	1.008	213.07	$-0.35^{+0.02}_{-0.02}$	$-2.10^{+0.03}_{-0.03}$	$434.48^{+14.07}_{-14.15}$	178.35	2468.1	$-0.61^{+0.01}_{-0.01}$	$524.01^{+16.30}_{-16.24}$	110.24	3082.47	-614.37
1.008	1.172	110.46	$-0.40^{+0.05}_{-0.05}$	$-2.19^{+0.06}_{-0.06}$	$367.26^{+23.03}_{-22.66}$	115.13	649.43	$-0.61^{+0.03}_{-0.03}$	$387.09^{+20.27}_{-20.13}$	72.5	729.02	-79.59
1.172	1.921	250.46	$-0.47^{+0.02}_{-0.02}$	$-2.30^{+0.03}_{-0.03}$	$364.12^{+9.48}_{-9.40}$	106.9	2915.46	$-0.64^{+0.01}_{-0.01}$	$367.53^{+8.93}_{-8.83}$	73.2	3248.94	-333.48
1.921	2.078	104.55	$-0.50^{+0.05}_{-0.05}$	$-2.32^{+0.08}_{-0.08}$	$286.95^{+16.71}_{-16.52}$	69.7	419.03	$-0.68^{+0.03}_{-0.03}$	$297.70^{+17.22}_{-17.37}$	47.5	476.94	-57.91
2.078	2.463	143.64	$-0.36^{+0.04}_{-0.04}$	$-2.15^{+0.04}_{-0.04}$	$221.87^{+10.13}_{-10.09}$	64.49	1722.38	$-0.66^{+0.02}_{-0.02}$	$260.37^{+10.33}_{-10.09}$	37.8	1875.05	-152.67
2.463	2.849	157.93	$-0.51^{+0.03}_{-0.03}$	$-2.25^{+0.05}_{-0.05}$	$295.65^{+12.67}_{-12.54}$	73.82	1813.37	$-0.69^{+0.02}_{-0.02}$	$314.59^{+12.76}_{-12.51}$	48.2	1949.14	-135.77
2.849	3.159	119.25	$-0.57^{+0.05}_{-0.05}$	$-2.26^{+0.07}_{-0.07}$	$259.66^{+16.17}_{-15.65}$	49.37	1300.49	$-0.75^{+0.03}_{-0.02}$	$293.17^{+15.12}_{-15.22}$	32.5	1355.46	-54.97
3.159	3.556	114.24	$-0.55^{+0.05}_{-0.05}$	$-2.19^{+0.06}_{-0.06}$	$190.54^{+11.27}_{-11.22}$	33.53	1573.62	$-0.80^{+0.03}_{-0.03}$	$238.38^{+13.62}_{-13.52}$	20.0	1651.65	-78.03
3.556	3.905	93.9	$-0.60^{+0.06}_{-0.06}$	$-2.28^{+0.08}_{-0.08}$	$182.74^{+11.97}_{-12.13}$	23.57	1246.25	$-0.81^{+0.03}_{-0.03}$	$217.83^{+14.30}_{-14.53}$	15.3	1285.31	-39.06
3.905	4.386	89.92	$-0.55^{+0.08}_{-0.08}$	$-2.12^{+0.06}_{-0.06}$	$156.45^{+13.47}_{-13.59}$	21.25	1685.38	$-0.86^{+0.04}_{-0.03}$	$224.93^{+16.59}_{-16.10}$	11.8	1736.74	-51.36
4.386	4.878	72.66	$-0.70^{+0.08}_{-0.08}$	$-2.15^{+0.08}_{-0.08}$	$157.93^{+15.93}_{-15.92}$	14.04	1650.0	$-0.97^{+0.04}_{-0.04}$	$244.94^{+23.45}_{-23.72}$	8.05	1679.4	-29.4
4.878	5.855	78.09	$-0.75^{+0.07}_{-0.07}$	$-2.41^{+0.14}_{-0.14}$	$164.70^{+13.75}_{-13.68}$	7.24	2533.13	$-0.88^{+0.04}_{-0.04}$	$183.12^{+14.69}_{-14.66}$	5.06	2547.54	-14.41
5.855	6.519	53.16	$-0.60^{+0.10}_{-0.10}$	$-2.28^{+0.13}_{-0.12}$	$135.87^{+13.28}_{-13.49}$	6.06	1836.63	$-0.85^{+0.06}_{-0.06}$	$163.89^{+18.28}_{-18.66}$	3.75	1852.18	-15.55
6.519	8.47	73.61	$-0.84^{+0.05}_{-0.05}$	$-2.47^{+0.15}_{-0.14}$	$180.81^{+11.74}_{-11.83}$	4.39	3434.79	$-0.92^{+0.04}_{-0.04}$	$198.40^{+16.87}_{-17.00}$	3.19	3448.67	-13.88
8.47	9.594	67.88	$-0.61^{+0.06}_{-0.06}$	$-2.13^{+0.08}_{-0.08}$	$207.45^{+15.68}_{-15.92}$	10.09	2693.48	$-0.80^{+0.04}_{-0.04}$	$247.71^{+21.19}_{-21.32}$	5.42	2725.47	-31.99
9.594	10.083	35.24	$-0.81^{+0.14}_{-0.14}$	$-2.07^{+0.20}_{-0.21}$	$208.97^{+51.72}_{-49.91}$	7.61	1424.88	$-0.96^{+0.06}_{-0.06}$	$291.76^{+45.79}_{-46.09}$	3.61	1437.42	-12.54
10.083	11.346	37.26	$-1.00^{+0.09}_{-0.09}$	$-2.25^{+0.25}_{-0.26}$	$206.89^{+37.08}_{-37.22}$	3.36	2684.86	$-1.08^{+0.06}_{-0.06}$	$277.93^{+44.64}_{-44.76}$	1.99	2691.42	-6.56
13.652	14.807	47.61	$-0.83^{+0.07}_{-0.07}$	$-2.18^{+0.14}_{-0.14}$	$225.54^{+25.82}_{-26.34}$	5.68	2628.19	$-0.96^{+0.05}_{-0.05}$	$292.08^{+38.30}_{-38.63}$	3.3	2641.13	-12.94
14.807	15.716	66.97	$-0.86^{+0.05}_{-0.05}$	$-2.31^{+0.15}_{-0.14}$	$238.77^{+22.26}_{-21.99}$	8.62	2384.08	$-0.95^{+0.04}_{-0.04}$	$287.80^{+27.73}_{-27.58}$	5.71	2395.35	-11.27
15.716	16.624	50.21	$-0.94^{+0.07}_{-0.07}$	$-2.55^{+0.23}_{-0.23}$	$158.62^{+15.61}_{-15.74}$	3.78	2314.14	$-1.02^{+0.06}_{-0.06}$	$187.58^{+24.90}_{-24.39}$	2.87	2319.26	-5.12
16.624	19.933	62.17	$-0.93^{+0.09}_{-0.09}$	$-2.26^{+0.13}_{-0.13}$	$115.98^{+13.11}_{-13.21}$	2.54	4089.06	$-1.09^{+0.04}_{-0.05}$	$169.93^{+19.06}_{-18.91}$	1.54	4107.09	-18.03
19.933	20.414	30.45	$-0.81^{+0.16}_{-0.16}$	$-2.54^{+0.27}_{-0.28}$	$120.73^{+18.56}_{-18.61}$	2.65	1302.6	$-0.95^{+0.11}_{-0.11}$	$139.61^{+27.80}_{-27.72}$	1.97	1306.19	-3.59
20.414	22.098	83.25	$-0.78^{+0.06}_{-0.06}$	$-2.40^{+0.10}_{-0.10}$	$130.48^{+7.68}_{-7.73}$	4.97	3285.78	$-0.93^{+0.04}_{-0.04}$	$151.82^{+11.72}_{-11.91}$	3.46	3315.72	-29.94
22.098	22.991	44.62	$-0.88^{+0.10}_{-0.10}$	$-2.73^{+0.22}_{-0.21}$	$98.14^{+7.86}_{-7.82}$	2.24	2266.88	$-0.99^{+0.08}_{-0.08}$	$109.19^{+15.81}_{-15.68}$	1.8	2270.88	-4.0
31.821	34.636	31.63	$-1.05^{+0.12}_{-0.12}$	$-2.74^{+0.29}_{-0.24}$	$102.95^{+12.10}_{-12.24}$	0.83	3794.2	$-1.13^{+0.09}_{-0.09}$	$133.40^{+25.80}_{-25.91}$	0.68	3793.86	0.34
35.169	35.633	38.92	$-0.94^{+0.06}_{-0.06}$	$-2.54^{+0.29}_{-0.30}$	$289.46^{+32.93}_{-32.92}$	6.06	1492.65	$-0.95^{+0.06}_{-0.06}$	$298.59^{+41.31}_{-42.07}$	4.49	1494.31	-1.66
35.633	36.354	38.32	$-0.86^{+0.08}_{-0.08}$	$-2.86^{+0.31}_{-0.31}$	$180.31^{+17.92}_{-18.21}$	2.88	1972.32	$-0.90^{+0.07}_{-0.07}$	$175.68^{+24.20}_{-24.39}$	2.48	1970.36	1.96
36.354	36.638	31.9	$-0.68^{+0.13}_{-0.14}$	$-2.43^{+0.24}_{-0.23}$	$142.74^{+18.71}_{-19.41}$	4.62	683.44	$-0.83^{+0.10}_{-0.10}$	$150.54^{+27.34}_{-27.45}$	3.06	687.04	-3.6
36.638	36.961	52.31	$-0.56^{+0.10}_{-0.10}$	$-2.25^{+0.13}_{-0.13}$	$178.78^{+19.23}_{-19.76}$	11.33	1081.59	$-0.79^{+0.06}_{-0.06}$	$210.28^{+25.90}_{-25.39}$	6.96	1097.6	-16.01
36.961	37.44	47.35	$-0.92^{+0.10}_{-0.10}$	$-2.51^{+0.24}_{-0.24}$	$169.29^{+23.96}_{-24.24}$	5.38	1552.48	$-1.03^{+0.06}_{-0.06}$	$212.09^{+30.22}_{-30.73}$	4.03	1559.1	-6.62
37.44	38.25	75.05	$-0.74^{+0.06}_{-0.06}$	$-2.70^{+0.18}_{-0.18}$	$141.42^{+8.41}_{-8.28}$	5.62	2240.16	$-0.82^{+0.05}_{-0.05}$	$134.20^{+10.14}_{-10.28}$	4.52	2247.91	-7.75
38.25	39.556	66.59	$-0.76^{+0.09}_{-0.09}$	$-2.46^{+0.14}_{-0.14}$	$100.32^{+8.08}_{-7.94}$	3.53	2905.42	$-0.96^{+0.05}_{-0.05}$	$121.76^{+11.72}_{-11.60}$	2.55	2920.88	-15.46
39.556	41.849	64.94	$-1.00^{+0.07}_{-0.07}$	$-2.31^{+0.12}_{-0.12}$	$123.41^{+11.25}_{-11.14}$	3.05	3676.57	$-1.14^{+0.05}_{-0.05}$	$187.30^{+21.62}_{-21.69}$	1.98	3693.33	-16.76
41.849	44.578	54.62	$-1.04^{+0.18}_{-0.17}$	$-2.41^{+0.26}_{-0.27}$	$92.25^{+19.47}_{-20.53}$	1.85	3815.0	$-1.25^{+0.05}_{-0.05}$	$168.82^{+23.58}_{-23.01}$	1.28	3873.71	-58.71
44.578	45.205	34.78	$-1.06^{+0.11}_{-0.11}$	$-2.84^{+0.22}_{-0.28}$	$98.25^{+9.71}_{-9.77}$	1.96	1733.51	$-1.11^{+0.10}_{-0.10}$	$120.29^{+21.62}_{-22.03}$	1.66	1732.15	1.36
45.869	46.996	56.31	$-0.91^{+0.13}_{-0.13}$	$-2.57^{+0.21}_{-0.22}$	$84.94^{+10.06}_{-10.13}$	2.58	2607.69	$-1.10^{+0.07}_{-0.07}$	$115.68^{+14.13}_{-14.22}$	1.94	2619.28	-11.59
46.996	47.344	51.11	$-0.78^{+0.08}_{-0.08}$	$-3.19^{+0.28}_{-0.28}$	$137.16^{+8.71}_{-8.78}$	4.83	1027.46	$-0.81^{+0.07}_{-0.07}$	$121.35^{+13.26}_{-13.39}$	4.4	1022.74	4.72
47.6	47.974	76.9	$-0.59^{+0.05}_{-0.05}$	$-2.82^{+0.22}_{-0.21}$	$193.50^{+10.54}_{-10.68}$	11.73	1421.85	$-0.65^{+0.04}_{-0.04}$	$158.08^{+10.83}_{-10.98}$	9.77	1424.93	-3.08
47.974	48.695	72.5	$-0.66^{+0.08}_{-0.08}$	$-2.44^{+0.12}_{-0.11}$	$115.31^{+8.12}_{-11.48}$	6.4	2157.85	$-0.88^{+0.05}_{-0.05}$	$132.80^{+11.43}_{-11.48}$	4.58	2177.07	-19.22
48.695	49.243	41.06	$-0.92^{+0.14}_{-0.14}$	$-2.43^{+0.19}_{-0.19}$	$90.52^{+10.76}_{-10.98}$	3.04	1640.68	$-1.13^{+0.10}_{-0.10}$	$134.34^{+26.46}_{-26.72}$	2.15	1651.54	-10.86
49.243	50.071	31.76	$-1.17^{+0.13}_{-0.14}$	$-2.53^{+0.29}_{-0.30}$	$111.41^{+20.29}_{-20.52}$	1.88	2164.14	$-1.26^{+0.09}_{-0.09}$	$178.14^{+40.32}_{-40.38}$	1.37	2169.89	-5.75
50.431	50.517	33.99	$-0.37^{+0.14}_{-0.04}$	$-2.21^{+0.19}_{-0.19}$	$252.46^{+41.02}_{-40.36}$	24.98	-670.88	$-0.62^{+0.08}_{-0.08}$	$269.88^{+39.72}_{-38.82}$	14.6	-663.99	-6.89
50.517	51.143	111.14	$-0.53^{+0.04}_{-0.04}$	$-2.65^{+0.15}_{-0.15}$	$256.88^{+11.36}_{-11.44}$	19.45	2254.79	$-0.59^{+0.03}_{-0.03}$	$203.12^{+9.53}_{-9.28}$	15.1	2272.57	-17.78
51.143	51.339	48.03	$-0.59^{+0.13}_{-0.13}$	$-2.12^{+0.11}_{-0.11}$	$134.42^{+17.36}_{-17.31}$	14.33	440.09	$-0.87^{+0.07}_{-0.07}$	$180.85^{+25.98}_{-26.03}$	7.31	465.91	-25.82
51.339	51.804	49.62	$-0.75^{+0.10}_{-0.10}$	$-2.55^{+0.21}_{-0.21}$	$132.36^{+12.90}_{-12.83}$	5.35	1493.78	$-0.88^{+0.07}_{-0.07}$	$140.52^{+16.14}_{-16.10}$	4.02	1500.38	-6.6
51.804	52.376	68.71	$-0.66^{+0.08}_{-0.08}$	$-2.63^{+0.16}_{-0.15}$	$116.88^{+7.27}_{-7.24}$	5.75	1853.42	$-0.79^{+0.06}_{-0.06}$	$112.55^{+9.95}_{-9.99}$	4.48	1867.32	-13.9

52.376	52.651	31.12	$-0.99^{+0.16}_{-0.17}$	$-2.66^{+0.27}_{-0.28}$	$87.95^{+11.95}_{-12.01}$	2.8	630.89	$-1.14^{+0.12}_{-0.12}$	$122.50^{+26.87}_{-27.16}$	2.23	633.62	-2.73
52.651	53.803	42.75	$-0.62^{+0.21}_{-0.20}$	$-2.38^{+0.13}_{-0.13}$	$62.61^{+7.18}_{-7.19}$	2.01	2655.99	$-1.04^{+0.09}_{-0.09}$	$92.16^{+14.01}_{-13.91}$	1.36	2694.36	-38.37
53.803	54.719	56.65	$-0.64^{+0.09}_{-0.09}$	$-2.83^{+0.18}_{-0.18}$	$93.91^{+4.75}_{-4.88}$	2.77	2387.05	$-0.74^{+0.07}_{-0.07}$	$82.11^{+7.84}_{-7.98}$	2.34	2394.05	-7.0
54.719	56.207	55.52	$-0.83^{+0.09}_{-0.09}$	$-2.94^{+0.23}_{-0.23}$	$77.76^{+4.40}_{-4.39}$	1.74	3054.06	$-0.91^{+0.07}_{-0.07}$	$77.23^{+7.80}_{-7.70}$	1.5	3055.92	-1.86
58.382	59.675	64.29	$-0.60^{+0.14}_{-0.14}$	$-2.64^{+0.15}_{-0.14}$	$63.29^{+4.54}_{-4.54}$	2.34	2832.41	$-0.90^{+0.07}_{-0.07}$	$69.32^{+6.58}_{-6.64}$	1.82	2859.66	-27.25
59.675	60.966	45.17	$-0.64^{+0.23}_{-0.23}$	$-2.56^{+0.14}_{-0.14}$	$45.87^{+4.25}_{-4.27}$	1.41	2723.52	$-1.11^{+0.11}_{-0.11}$	$66.40^{+10.45}_{-10.29}$	1.08	2789.89	-66.37
60.966	61.509	38.74	$-0.54^{+0.17}_{-0.16}$	$-3.10^{+0.23}_{-0.24}$	$55.32^{+3.23}_{-3.21}$	1.66	1541.7	$-0.72^{+0.13}_{-0.13}$	$47.45^{+6.22}_{-6.29}$	1.47	1538.24	3.46
61.509	62.273	35.2	$-0.75^{+0.27}_{-0.26}$	$-2.62^{+0.16}_{-0.16}$	$41.18^{+3.98}_{-3.87}$	1.31	1948.82	$-1.21^{+0.14}_{-0.14}$	$66.40^{+13.36}_{-13.28}$	1.01	2008.03	-59.21
62.273	63.528	30.68	$-0.46^{+0.28}_{-0.28}$	$-2.54^{+0.13}_{-0.13}$	$37.16^{+3.30}_{-3.34}$	0.88	2601.14	$-1.24^{+0.14}_{-0.14}$	$69.83^{+15.71}_{-15.51}$	0.68	2667.76	-66.62

Table B2. Joint *Swift* BAT, *Fermi* GBM, and ASIM spectral analysis results of the bright emission pulse of GRB 210619B using Band and CPL functions. Flux values (in erg cm^{-2} s^{-1}) are calculated in 8 keV-40 MeV energy range. T$_{start}$ and T$_{stop}$ have been referred with respect to the ASIM reference time (T$_{0,\,ASIM}$).

T$_{start}$ (s)	T$_{stop}$ (s)	α_{pt}	β_{pt}	E_p (keV)	(Flux $\times10^{-06}$)	DIC$_{Band}$	Γ_{CPL}	E_c (keV)	(Flux $\times10^{-06}$)	DIC$_{CPL}$	Δ DIC
0.00	1.00	$-0.30^{+0.07}_{-0.07}$	$-1.71^{+0.04}_{-0.04}$	$496.39^{+44.58}_{-44.66}$	29.75	2534.26	$-0.57^{+0.03}_{-0.03}$	$750.30^{+58.77}_{-59.56}$	12.02	2672.69	-138.43
1.00	1.70	$-0.40^{+0.02}_{-0.02}$	$-2.13^{+0.02}_{-0.02}$	$460.65^{+15.80}_{-15.71}$	127.40	3197.60	$-0.66^{+0.01}_{-0.01}$	$692.86^{+20.58}_{-20.13}$	74.69	3756.60	-559.0
1.70	2.18	$-0.54^{+0.02}_{-0.02}$	$-2.32^{+0.03}_{-0.03}$	$412.58^{+15.98}_{-15.92}$	84.11	2201.97	$-0.71^{+0.01}_{-0.01}$	$491.75^{+15.28}_{-15.85}$	55.75	2479.64	-277.67
2.18	2.79	$-0.56^{+0.02}_{-0.02}$	$-2.42^{+0.04}_{-0.04}$	$345.77^{+10.54}_{-10.42}$	61.94	2504.32	$-0.70^{+0.01}_{-0.01}$	$367.59^{+11.24}_{-10.97}$	43.98	2746.71	-242.39
2.79	3.60	$-0.55^{+0.02}_{-0.02}$	$-2.29^{+0.03}_{-0.03}$	$268.83^{+8.12}_{-7.98}$	47.81	2898.92	$-0.74^{+0.01}_{-0.01}$	$323.73^{+9.97}_{-9.84}$	33.03	3221.45	-322.53
3.60	4.50	$-0.64^{+0.03}_{-0.03}$	$-2.28^{+0.04}_{-0.04}$	$211.83^{+7.69}_{-7.68}$	20.07	2712.79	$-0.84^{+0.02}_{-0.02}$	$270.66^{+10.82}_{-10.96}$	15.55	2873.18	-160.39

Table B3. The results of energy-resolved spectral lag analysis for GRB 210619B. We considered 15-25 keV and 8-30 keV energy channels as a reference light curve for the *Swift* BAT and *Fermi* GBM observations, respectively. The each lag values is calculated for 50000 numbers of simulations to fit the cross-correlation function.

Swift BAT		*Fermi* GBM	
Energy range (keV)	**Spectral lag (ms)**	**Energy range** (keV)	**Spectral lag (ms)**
25-50	$-38.28^{+73.46}_{-73.51}$	30–50	$-37.16^{+68.89}_{-68.66}$
50-100	$-160.25^{+66.53}_{-66.42}$	50–100	$-95.46^{+61.31}_{-60.67}$
100-200	$-239.73^{+46.26}_{-46.06}$	100–150	$-207.11^{+60.83}_{-60.08}$
200-350	$-386.78^{+37.23}_{-36.90}$	150–200	$-308.86^{+50.02}_{-49.87}$
		200-250	$-378.55^{+44.84}_{-44.99}$
		250–300	$-405.58^{+44.32}_{-43.91}$
		300–400	$-473.87^{+32.98}_{-32.91}$
		400–500	$-545.70^{+32.09}_{-31.87}$
		500–600	$-555.08^{+27.65}_{-27.89}$
		600–700	$-579.31^{+27.29}_{-27.19}$
		700–800	$-511.07^{+26.40}_{-26.68}$
		800–900	$-786.49^{+21.37}_{-21.40}$

This paper has been typeset from a TEX/LATEX file prepared by the author.

Table B4. Our optical observations log of GRB 210619B. No extinction corrections are applied in the reported magnitude values.

Start time (UT)	End time (UT)	Exposure (s)	Filter	Mag	error	Telescope
$2021-06-20T14:20:15.554$	$2021-06-20T15:06:12.596$	60×15	Clear	> 18.54	nan	BOOTES-4
$2021-06-20T22:40:39.21$	$2021-06-20T23:05:57.03$	90×5	B	> 20.76	nan	OSN
$2021-06-20T22:42:16.57$	$2021-06-20T23:07:40.52$	90×5	V	20.54	0.20	OSN
$2021-06-20T22:33:32.16$	$2021-06-20T22:39:39.78$	90×4	R	19.52	0.12	OSN
$2021-06-20T22:43:54.15$	$2021-06-20T23:09:24.76$	90×5	I	18.94	0.12	OSN
$2021-06-22T02:07:27.55$	$2021-06-22T02:54:19.07$	300×5	R	20.87	0.11	OSN
$2021-06-22T02:12:36.78$	$2021-06-22T02:59:26.09$	300×5	I	20.59	0.17	OSN
$2021-06-22T23:16:32.19$	$2021-06-23T01:03:12.29$	300×9	R	21.93	0.20	OSN
$2021-06-22T23:21:42.05$	$2021-06-23T01:08:24.00$	300×9	I	21.15	0.17	OSN
$2021-06-24T23:35:35.23$	$2021-06-25T00:27:24.91$	300×10	I	21.77	0.46	OSN
$2021-06-27T02:59:56$	$2021-06-27T03:25:28$	180×6	r	23.04	0.29	CAHA
$2021-06-25T04:12:48.732$	$2021-06-25T04:16:19.954$	20×2	r	22.21	0.12	GTC
$2021-07-10T03:17:43.533$	$2021-07-10T03:40:05.462$	90×12	g	25.74	0.26	GTC
$2021-07-10T03:40:36.943$	$2021-07-10T04:02:59.557$	90×12	r	24.75	0.26	GTC
$2021-07-10T04:03:31.040$	$2021-07-10T04:18:53.471$	60×12	i	23.89	0.09	GTC
$2021-07-10T04:20:25.973$	$2021-07-10T04:32:21.711$	50×10	z	23.85	0.21	GTC
$2021-07-30T02:56:04.292$	$2021-07-30T03:18:26.445$	90×12	g	>26.7	nan	GTC
$2021-07-30T03:18:56.263$	$2021-07-30T03:40:18.501$	90×12	r	>25.7	nan	GTC
$2021-07-30T03:41:48.283$	$2021-07-30T03:58:09.245$	60×12	i	>26.4	nan	GTC
$2021-07-30T03:58:40.515$	$2021-07-30T04:10:35.009$	50×10	z	>24.8	nan	GTC

Table B5. The optical observations log of GRB 210619B taken from literature. No extinction corrections are applied in the reported magnitude values (in AB system).

T$_{\mathbf{mid}}$ (s)	Magnitude	Filter	Telescope	References
9307	18.58 ± 0.03	g	Liverpool	Perley (2021)
13755	18.93 ± 0.03	g	Liverpool	Perley (2021)
72180	21.14± 0.07	g	GIT	Kumar et al. (2021)
65700	21.13 ± 0.07	g	GIT	Kumar et al. (2021)
2771	17.80 ± 0.05	g	D50	Oganesyan et al. (2021)
2902	17.93 ± 0.06	g	D50	Oganesyan et al. (2021)
3061	17.87 ± 0.05	g	D50	Oganesyan et al. (2021)
5384	18.14 ± 0.10	g	D50	Oganesyan et al. (2021)
13848	18.11± 0.03	r	Liverpool	Perley (2021)
9399	17.82 ± 0.03	r	Liverpool	Perley (2021)
1318	16.10 ± 0.10	r	Liverpool	Shrestha et al. (2021)
67284	20.18 ± 0.05	r	GIT	Kumar et al. (2021)
22104	18.52 ± 0.12	r	REM	D'Avanzo et al. (2021b)
84154	20.50 ± 0.40	r	iTelescope	Romanov (2021)
236914	21.82 ± 0.26	r	AZT-20	Belkin et al. (2021b)
256068	21.45 ± 0.33	r	RC80	Vinko et al. (2021)
529067	22.56 ± 0.16	r	CAHA	Kann et al. (2021b)
3442	17.20 ± 0.05	r	D50	Oganesyan et al. (2021)
3505	17.20 ± 0.06	r	D50	Oganesyan et al. (2021)
3569	17.19 ± 0.06	r	D50	Oganesyan et al. (2021)
3633	17.30 ± 0.06	r	D50	Oganesyan et al. (2021)
3696	17.30 ± 0.07	r	D50	Oganesyan et al. (2021)
3760	17.29 ± 0.06	r	D50	Oganesyan et al. (2021)
3823	17.23 ± 0.06	r	D50	Oganesyan et al. (2021)
3886	17.27 ± 0.06	r	D50	Oganesyan et al. (2021)
5799	17.57 ± 0.08	r	D50	Oganesyan et al. (2021)
5988	17.57 ± 0.09	r	D50	Oganesyan et al. (2021)
6177	17.56± 0.10	r	D50	Oganesyan et al. (2021)
84656	20.16 ± 0.19	r	D50	Oganesyan et al. (2021)
163842	21.12 ± 0.48	r	D50	Oganesyan et al. (2021)
9490	17.44 ± 0.04	i	Liverpool	Shrestha et al. (2021)
13939	17.74 ± 0.04	i	Liverpool	Shrestha et al. (2021)
3952	16.88 ± 0.05	i	D50	Oganesyan et al. (2021)
4014	17.05 ± 0.07	i	D50	Oganesyan et al. (2021)
4078	16.93 ± 0.06	i	D50	Oganesyan et al. (2021)
4142	17.00 ± 0.07	i	D50	Oganesyan et al. (2021)
4206	16.91± 0.07	i	D50	Oganesyan et al. (2021)
4271	17.00 ± 0.07	i	D50	Oganesyan et al. (2021)
4335	17.03 ± 0.07	i	D50	Oganesyan et al. (2021)
4399	17.01 ± 0.08	i	D50	Oganesyan et al. (2021)
4462	17.02 ± 0.08	i	D50	Oganesyan et al. (2021)
14149	17.47 ± 0.04	z	Liverpool	Shrestha et al. (2021)
9700	17.17 ± 0.04	z	Liverpool	Shrestha et al. (2021)
4589	16.77 ± 0.06	z	D50	Oganesyan et al. (2021)
4781	16.81 ± 0.08	z	D50	Oganesyan et al. (2021)
4971	16.68 ± 0.06	z	D50	Oganesyan et al. (2021)
6865	16.90 ± 0.11	z	D50	Oganesyan et al. (2021)
9498	17.90 ± 0.20	V	iTelescope	Kong (2021)
51948	19.21 ± 0.10	R	TNT	Xin et al. (2021)
85679	20.01 ± 0.10	R	SAO RAS	Moskvitin et al. (2021a)
81215	20.11 ± 0.20	R	OSN	Hu et al. (2021)
241580	21.42 ± 0.09	R	AZT-22	Belkin et al. (2021b)
593153	22.76 ± 0.24	R	AZT-22	Belkin et al. (2021b)
1111648	23.71 ± 0.30	R	AZT-22	Belkin et al. (2021b)
69088	19.68 ± 0.06	R	AZT-22	Belkin et al. (2021b)
159856	20.64 ± 0.05	R	AZT-22	Belkin et al. (2021b)
102244	20.13 ± 0.02	R	NOT	Zhu et al. (2021)
171876	20.81 ± 0.30	R	AS-32	Belkin et al. (2021a)
171289	20.94 ± 0.08	R	SAO RAS	Moskvitin et al. (2021b)
99792	20.21 ± 0.20	R	Schmidt-Cassegrain	Romanov & Lane (2021)
255989	21.61 ± 0.10	R	SAO RAS	Moskvitin et al. (2021c)
5042	16.75 ± 0.05	I	CAHA	Kann et al. (2021a)
13373	17.45 ± 0.05	I	CAHA	Kann et al. (2021a)